Doctoral Dissertations and Master's Theses

Fall 12-2020

Analysis of After Impact Characteristics and Structural Optimization of CFRP Composite Plate

Zhennan He
Embry-Riddle Aeronautical University

Follow this and additional works at: https://commons.erau.edu/edt

Part of the Structures and Materials Commons

Scholarly Commons Citation

He, Zhennan, "Analysis of After Impact Characteristics and Structural Optimization of CFRP Composite Plate" (2020). *Doctoral Dissertations and Master's Theses*. 555.
https://commons.erau.edu/edt/555

This Thesis - Open Access is brought to you for free and open access by Scholarly Commons. It has been accepted for inclusion in Doctoral Dissertations and Master's Theses by an authorized administrator of Scholarly Commons. For more information, please contact commons@erau.edu.

ANALYSIS OF AFTER IMPACT CHARACTERISTICS AND STRUCTURAL

OPTIMIZATION OF CFRP COMPOSITE PLATE

By

Zhennan He

A Thesis Submitted to the Faculty of Embry-Riddle Aeronautical University

In Partial Fulfillment of the Requirements for the Degree of

Master of Science in Aerospace Engineering

December 2020

Embry-Riddle Aeronautical University

Daytona Beach, Florida

ANALYSIS OF AFTER IMPACT CHARACTERISTICS AND STRUCTURAL
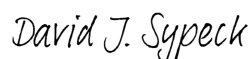OPTIMIZATION OF CFRP COMPOSITE PLATE

By

Zhennan He

This Thesis was prepared under the direction of the candidate's Thesis Committee
Chair, Dr. Mandar Kulkarni, Department of Aerospace Engineering, and has been
approved by the members of the Thesis Committee. It was submitted to the
Office of the Senior Vice President for Academic Affairs and Provost,
and was accepted in the partial fulfillment of the requirements for
the Degree of Master of Science in Aerospace Engineering.

THESIS COMMITTEE

Chairman, Dr. Mandar Kulkarni	Member, Dr. Marwan Al-Haik

Member, Dr. David J. Sypeck

12/3/2020

Graduate Program Coordinator,   Date
Dr. Marwan Al-Haik

12/4/2020

Dean of the College of Engineering,   Date
Dr. Maj Mirmirani

12/4/2020

Associate Provost of Academic Support,   Date
Dr. Christopher Grant

ACKNOWLEDGEMENTS

First of all, I would like to express my great gratitude to Dr. Mandar Kulkarni who has brought me into the project and provided me continuous help through this research journey. I would never forget those weekly meetings whenever I had any questions or ideas, he would patiently give me elaborate answers and feasible planning for the next steps. Also, he would always make a quick response to me through endless email communication. His erudition and great enthusiasm helped me conquer the challenges and impel my thesis forward till completion.

Special thanks to Dr. David Sypeck for spending months training me getting familiar with the testing equipment and helped me to finish the low-velocity impact test and understand the technique of the compression test. Without his help, my research would be stuck at the beginning. Also, I want to thank Dr. Marwan Al-Haik who helped me learn the X-Ray imaging testing and understand the failure mechanism of composite materials. I am also grateful to Dr. Sirish Namilae who providing the equipment and tools for the laminates fabrication. Besides, I must thank Christian Aparicio from MSC Corporation for giving me the professional guidance of optimization methods.

At last, my greatest gratitude gives to my dear parents and my close friends. Whenever I'm feeling down, they are always my best confessors and confidants. Their care and understanding help me regain confidence and be able to achieve my dream.

ABSTRACT

Low-velocity impact (LVI) on composites may cause Barely Visible Impact Damage (BVID), which is one of the most common damage types and may result in a decrease in strength of the composite. The objectives of this research were (a) to identify the characteristics of a carbon/epoxy composite plate after low-velocity impact, (b) to create a validated model to simulate the impact process and progressive failure, and (c) to perform sizing and shape optimization of the laminate for improving the damage resistance of the plate. As a part of this thesis, composite plates were fabricated using carbon fiber reinforced polymer (CFRP) prepreg. The LVI testing was performed on the samples with different impactors and different impact energy levels. The X-Ray Micro-tomography technique helped to reveal the internal fiber damage and matrix damage of the impacted plate. Numerical models with nonlinear dynamic responses were developed in ABAQUS, which validated the LVI experiments. Further, the modified model was created in MSC. PATRAN/NASTRAN to optimize the ply thickness, ply orientation, and dimensional properties of the plate to minimize the weight while abiding by the structural response constraints. Moreover, the possibility of the OpenMDAO framework in nonlinear dynamic analysis and size optimization was explored.

TABLE OF CONTENTS

LIST OF FIGURES

Figure   Page

LIST OF TABLES

NOMENCLATURE

ACT	Advanced composites technology
BVID	Barely visible impact damage
CAI	Compressive after impact
CDM	Continuum damage mechanics
CFRP	Carbon fiber reinforced polymer
CLT	Classical laminate theory
CZM	Cohesive zone modeling
DOF	Degrees-of-freedom
ESLs	Equivalent static loads
FEA	Finite element analysis
FEM	Finite element method
LVI	Low-velocity impact
MAUD	Modular analysis and unified derivatives
MDO	Multidisciplinary design optimization
MMFD	Feasible directions
MPCs	Multi-point constraints
NDE	Non-destructive damage evaluation
NDT	Non-destructive technique
NLP	Nonlinear programming
PCL	Patran command language
RFI	Resin film infusion
RSM	Response surface method

SLP	Sequential linear programming
SQP	Sequential quadratic programming
UD	Unidirectional
VCCT	Virtual crack closure technique
VID	Visible impact damage
VUMAT	User-defined material subroutine
C_d	Damaged elasticity matrix
d_f, d_m, d_s	Damage variables
E_a	Absorbed energy
E_e	Elastic energy
G_c	Fracture energy dissipation
C	Compressive strength
CPU	Central processing unit
E	Impact energy
E_{11}, E_{22}, E_{33}	Elastic modulus
E_f	Young's modulus of the fiber
E_m	Young's modulus of the matrix
F	Contact force
FI	Failure index
G_{23}	Shear modulus
k	Wavenumbers in the principal direction
KE (t)	Kinetic energy
L	Length

m	Mass
M	Damage matrix
Q	Stiffness matrix
R	Wave amplitude
R	Residual functions
RAM	Random-access memory
S	In-plane shear strength
SOL	Solution
T	Tensile strength
t	Time
T	Total thickness
U, δ	Displacement
v	Velocity
v_{12}, v_{13}, v_{23}	Poisson's ratios
v_f	Volume fraction of fiber
v_m	Volume fraction of matrix
W	Width
X	Allowable strength in the longitudinal direction
Y	Allowable strength in the transverse direction
α	A coefficient
ε	Strain
ρ	Density
σ	Contact stress

$\hat{\sigma}$ Effective stress tensor

σ_{ij} Stresses rotated to the fracture plane

δ^f_{eq} Displacement when a damage mode completed

ψ Vector

ω Angular frequency

1. Introduction

Composite materials are made from two or more constituent materials with different physical and chemical properties, and the improved properties of their base materials bring the specialization to do a certain job, for instance, to make the structure stronger, lighter, or more suitable for manufacturing. Because the composite material in such a mixed state weakens some performance deficiencies of component materials, makes its component complement each other, and improves the comprehensive performance of the material, so it can be used in the structure with clear loading conditions and improve its overall performance.

Compared with traditional materials, carbon fiber composite has the following advantageous characteristics in design and manufacture: 1. Design structure is consistent with the composite material. 2. Structure can be designed freely by users for better strength and stiffness. 3. Ratio of the constituents could be adjusted according to needs. In recent years, composite materials have been widely used in aerospace, automotive industry, mechanical manufacturing, and medical fields, showing its bright application potential. The increased usage of composite material in aircraft is shown in Figure 1.1.

1.1. Background

With the improvement of the utility ratio of composite materials to metal material in aircraft, the application range of composite materials has gradually extended from some small and unimportant parts to load-bearing structures, such as the keel frame of the Airbus A340 - 600 (Toulouse, France), an integral structure, like the aircraft frame and wings (Kassapoglou, 2013). Figure 1.2 compares the overall efficiency of carbon/epoxy

and aluminum materials and shows good corrosion and fatigue ability of composites.

Among all the composites, the lightweight and high performance of Carbon Fiber

Reinforced Polymer (CFRP) structures are attractive that can benefit from weight saving,

high specific strength, and stiffness (Campbell, 2006). The following are examples of

CFRP composites being applied to commercial aircraft.
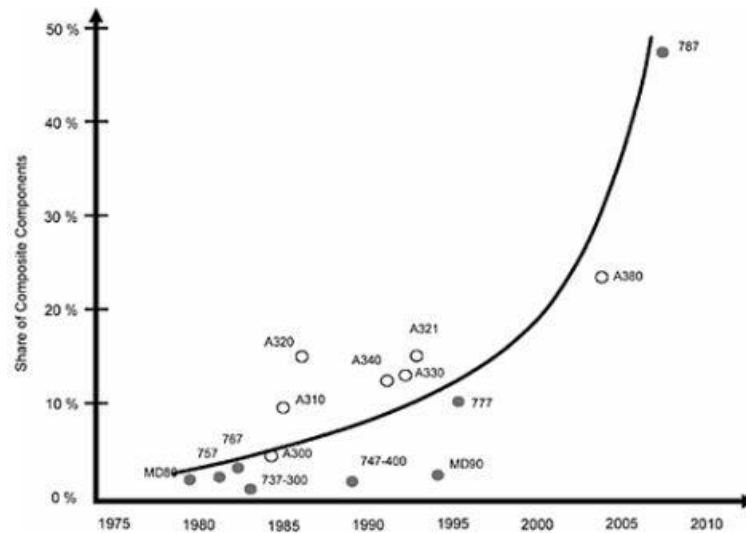
Figure 1.1 Percentage of composite components in commercial aircraft (Jom, 1989).

For instance, the Boeing (Chicago, Illinois) 7E7 series, as the 787 Dreamliner shown

in Figure 1.3 (Alemour et al., 2019), contains a higher proportion of polymer matrix

composite materials in its structure than any other equivalent aircraft, which allow it to

achieve the desired life-safety requirement and certain working condition at a lower

structural weight. Also, the vertical stabilizer mounted on Airbus A310 is a primary

aerodynamic structure and is entirely fabricated from the CFRP composites, which saves

400 kg after abandoning the Al alloy it used before. Besides, the CFRP fin box only has

95 small parts which is far less time consuming to produce and assemble when

comparing with more than 2000 parts that are made from metal.
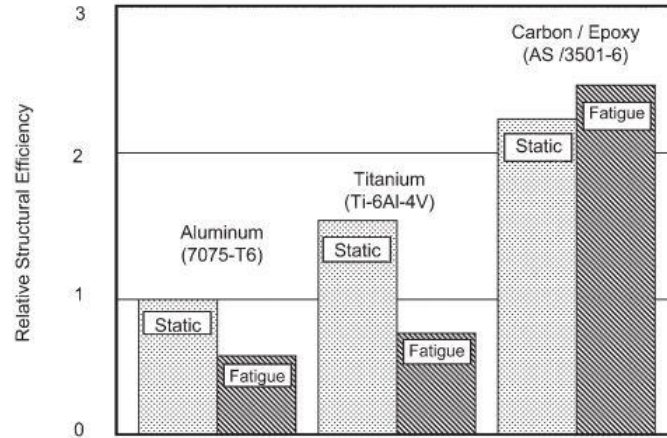
Figure 1.2 Relative structural efficiency of aerospace materials (Campbell, 2006).

Based on the advantages of the CFRP composite, further explores its great potential in reducing manufacturing time cost is necessary, and it is becoming a challenging task for the aircraft manufacturer to overcome. The resin film infusion (RFI) process accompany with the Advanced Composites Technology (ACT) programming, decreases the resin being used. If using radiation with a thermal oven rather than the traditional heat source, the curing process would save 90% of the time and hence 50% cost comparing with the use of an autoclave. Another example is the V22 from Bell Textron (Fort Worth, Texas). By replacing the thousands of fasteners with bonding joints and less costing jigging, the assembly cost is greatly decreased (Scoutis, 2005).
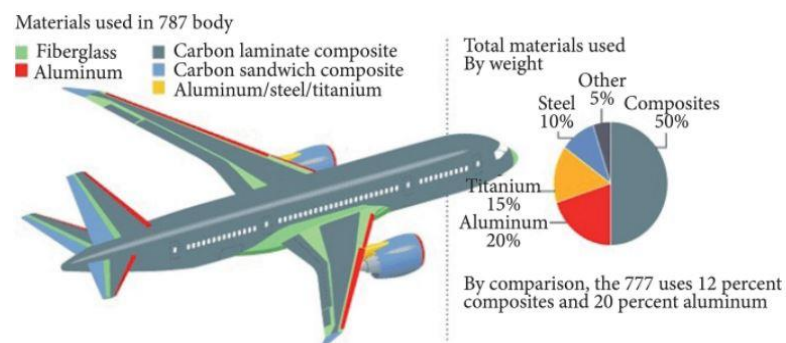
Figure 1.3 Utility of various materials in Boeing 787 Dreamliner (Alemour et al., 2019).

1.2. Effect of LVI

Composite materials are generally vulnerable to plane impact, which often happens during fabrication, during assembly, and in service. Many events can cause impact damage to composites, such as metal debris, tool drop, and even bird strike. In some situations, the impactor objective has high mass, but low velocity, and the resulting damage area may always invisible during visual inspection.

The main area of the impact could be on the wings, fuselage, and nose, etc. Unlike metal, which would display some forms of visible surface damage, composite impact damage often occurs as internal damage with complex types of failure modes. Due to the anisotropic properties of laminates, and unevenly distributed stresses inside or outside the laminae under the nonlinear transient dynamic loading, progressive damages could vary, depending on the loading condition and mechanical property of the material (Sun et al., 2018). When the intra-laminar begins among a single ply, the damage initiation wouldn't lead to the failure of the structure.

The structure wouldn't collapse until the damage or crack expends to several plies even whole laminates, and such progress is shown in Figure 1.4. In general, researchers divide different impact cases into low-velocity impact, high-velocity impact, and even hypervelocity impact, basing on the defined impact speed. Although there's no clear definition and boundary of these types, researchers make judgments by their experience which depends on the real situation. Also, the severity of damage increases at higher impact speed or energy. Accordingly, when the surface of the composite structure is struck at different energy levels, the barely visible impact damage (BVID) and/or visible impact damage (VID) could appear (Hampson & Moatamedi, 2007).
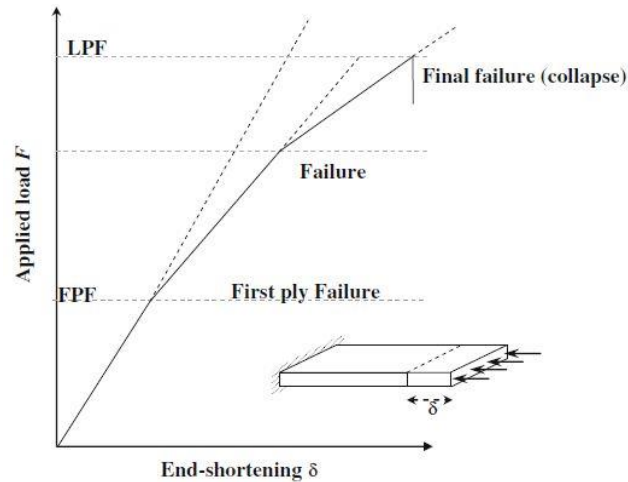
Figure 1.4 Progressive failure process of a ply (Pietropaoli & Pietropaoli, 2012).

For instance, different damage mechanisms of a quasi-isotropic carbon fiber, Tenax HTS45, NCF composite which was hit at low impact energy (15 J), is shown in Figure 1.5. In this research, the study of the low-velocity impact and BVID are the main scopes, which help to discover the after impact characteristics of the composite.

In most cases, the BVID, which is a non-catastrophic, is one of the most common damage types and accounts for nearly 80% of all aircraft damages (Cook et al., 2012). The BVID will result in sudden stiffness drop and strength degradation. Around 70% of the residual compression stress may be lost compared to the undamaged one. Because such impact damage on aircraft results in potential threats to air safety, it is important to assess the after-impacted composite structure for surface and internal damage during inspection, and also be able to predict possible damage location and severity once the impact occurs. Therefore, study the failure mechanism of the composite material is vital and methods of improving damage tolerance are one focus of this research.
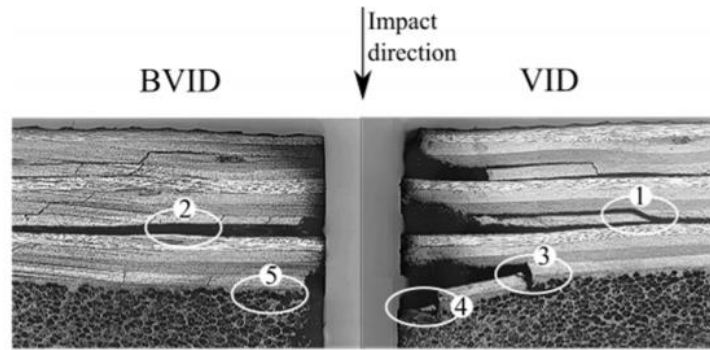
Figure 1.5 Microscopy image of BVID and VID damages. 1. Transverse shear crack 2. Delamination 3. Fiber breakage 4. Core crushing 5. Face sheet debonding (Raju et al., 2008).

1.3. Progressive Failure of LVI

Energy absorption of an impact is large most of the time, and through the process, energy is dissipated into different forms of damage. For a fiber-reinforced composite like CFRP, fiber fracture/splitting, matrix fracture, and fiber/matrix debonding are dominated by intra-laminar damages, while delamination is a phenomenon of interlaminar damage (Kreculj & Rasuo, 2013). For unidirectional laminates, the possible damage types are illustrated in Figure 1.6 (Birur, 2008).

On the whole, low-velocity impact often happens over a longer time, which creates global deformation through the thickness direction. Since the impact force is not as localized as a high-velocity impact, the contact time is relatively longer for the low-velocity impact scenario. Moreover, there is always damage observed far from the impact area (Farooq & Gregory, 2009). These types of damages all accumulate during the impact and cause a drop in load-carrying ability. Note that the type of composite studied in this research is thin unidirectional laminate made from thin plies (< 2 mm), although most prior studies investigated were standard laminates (≈ 4 mm, as mentioned in ASTM D7136 / D7136M-15) or thick laminate (> 4 mm) made from thin plies.
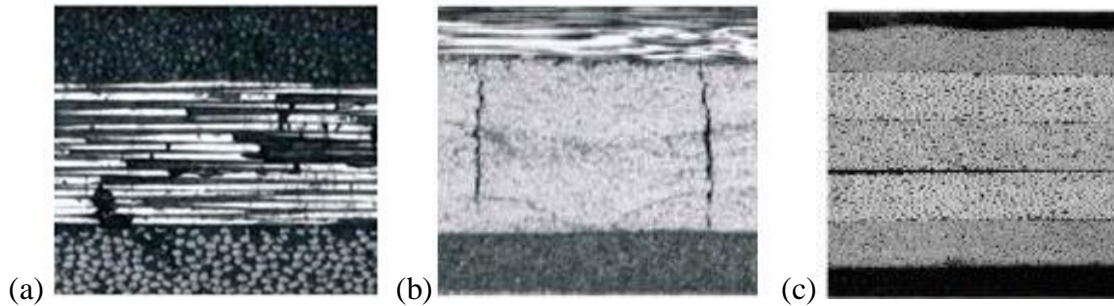
Figure 1.6 a) Fiber fracture, b) Transverse matrix crack, and c) Delamination (Birur, 2008).

So, it is necessary to study the mechanical response and failure of thin plies and thin laminate, which is being used widely for current in-service aircraft. Thus, this research focuses on the failure mechanisms of thin laminate. Besides, thin laminates are more vulnerable compared to thick laminates under direct impact, and the simulation of such a process is more complex. Laminates can be defined as thin or thick. For a thin laminate, layers that build the laminate could be classified as thin plies or thick plies, depending on the standard the researchers use (Sasikumar et al., 2019). Regarding ply thickness, Yokozeki, and Ogasawara (2008) reported that laminates with thickness between 3.6 mm and 4.4 mm, the one with thin plies would have an average of 20% compressive after impact (CAI) strength improvement compared to the one with thick plies.

Moreover, thin plies showed better performance than thick plies that it could delay the damage initiation (Guillamet et al., 2014). Other than the ply thickness, the total thickness of the laminate has a greater effect on the CAI itself. In a certain case (García-Rodríguez, 2018), when the laminate is less thick, as the 2.15 mm thick fabric laminate studied by the CAI strength, there was an increase of 27% if using thin plies rather than the standard plies.

A thin laminate shows quasi-brittle failure under impact and thicker laminates contain matrix crushing and delamination as main forms of damages. Thin laminate has less bending stiffness, so during an impact event, there will be enormous bending forces on them, which will be transformed into plane stresses. Therefore, fiber splitting is likely on the backside of an impacted laminate. Thus, under low-velocity impact, a thin laminate with thin plies shows fiber breakage/splitting, deep permanent indentation, and larger dissipated energy.

Note that any fiber damage would appear much later than matrix cracking and delamination. Here, different fiber failure patterns of in-plane and out-of-plane are illustrated in Figure 1.7 and Figure 1.8 (Carrere & Marie, 2013), for a typical unidirectional (UD) ply. Here, the angle $\pm\alpha$ in Figure 1.8 (b) and (c) denotes that when failure is due to compression, the angles of the fracture planes 3-2 and 2-3, concerning the 2 and 3 axes. The main damage in thick laminates is delamination damage. Matrix damage is always realized by the mismatching behavior between the fiber and matrix. In UD plies, matrix crack expansion would be parallel to the fiber direction. The matrix cracking causes delamination damage.
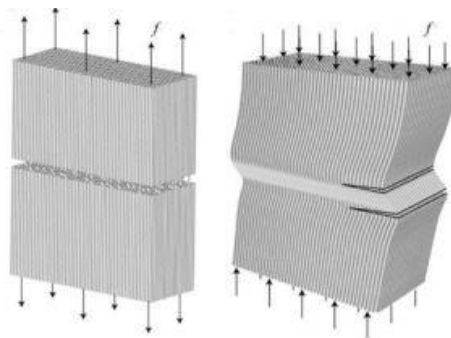
Figure 1.7 Fiber failure mechanisms of a UD ply: longitudinal tensile failure (left) and longitudinal compressive failure due to fiber kinking (right) (Carrere & Marie, 2013).
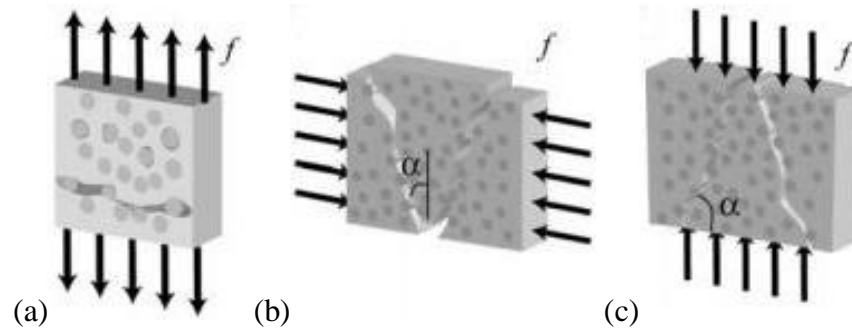
Figure 1.8 Inter-fibre failure mechanisms of a UD ply: a) tensile failure in the thickness direction, b) transverse compressive failure, and c) compressive failure in the thickness direction (Carrere & Marie, 2013).

This matrix crushing has been observed in the initial stage of the intra-laminar damage before other types of damage appear. Matrix crushing decreases the stiffness of the structure that gradually leads to a decrease in the load-capacity of the laminate. A schematic diagram of the matrix under compression and tension is shown in Figure 1.9.
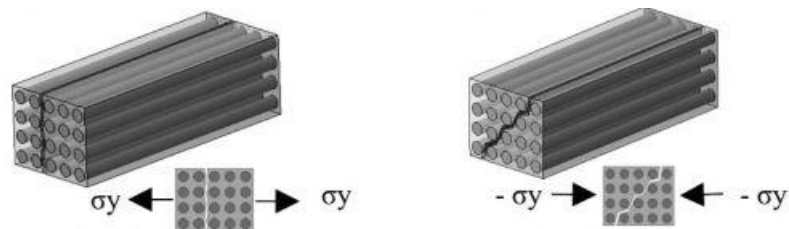
Figure 1.9 Schematic diagram of matrix damage (Shah et al., 2019).

For delamination, damage is due to bending stiffness variation between nearby plies. The damaged area has a peanut shape, and the shape and size of such inter-ply delamination are demonstrated in Figure 1.10 (Maio et al., 2013). The size, shape, and orientation of delamination would be affected by fiber direction within layers. As for related damage mechanism: When the impact body acts on the laminate, the laminate is bent and deformed, and its backside tensile stress is largest because the transverse tensile

strength of the composite material is less than the longitudinal tensile strength, which causes tensile failure of the matrix on the back of the laminate to evolve along the fiber direction; at the same time, the cracks develop along the thickness direction toward the impact surface, causing delamination failure when reaching the interlayer.

To ease damage due to impact damage, it is necessary to access damage resistance of the laminate and try to improve its capability of resisting impact damage. In testing, residual strength, especially for the compressive after impact strength, marked the ability of damage resistance and damage tolerance of the composite (Xiaoquan et al., 2009).
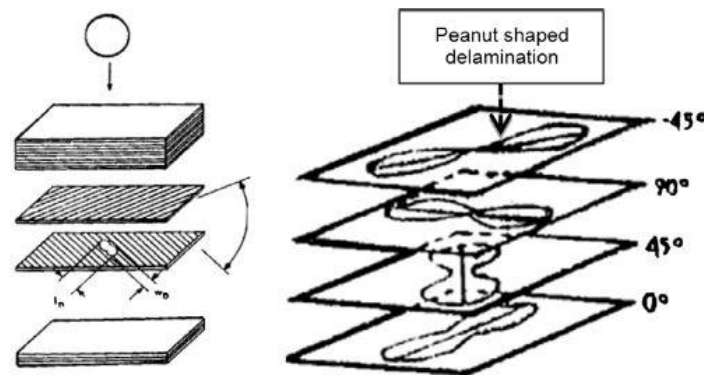
Figure 1.10 Delamination after impact and the typical damage shape among the plies (Maio et al., 2013).

1.4. Motivation and Scope of the Thesis

The low-velocity impact damage often happens to the aircraft during fabrication, maintenance, or in-service operations. It causes potential threats to air safety. So, the motivation of this research is to investigate after-impacted characteristics and internal damage of a composite structure through experimental and numerical methods. Therefore, some damage can be avoided before catastrophic danger occurs. Also, the cost is an important part when designing the CFRP structure.

Thus, another research significance is to develop the structure that becomes lighter to decrease the cost while maintaining the structural strength. Therefore, the final step is to optimize the properties of the composite structure that gives better damage tolerance.

In Chapter 2, the literature survey of prior studies on LVI will be mentioned and the discovery from the experiments will be provided. Also, the possible simulation techniques of LVI used along with the experiments will be introduced and compared. At last, the expressions of composite failure criteria: mode-dependent failure theory, and model-independent failure theory will be discussed.

Chapter 3 is based on the results of 3 sets of experiments and the results will be presented and findings will be discussed. First, several CFRP composite flat plate will be fabricated for the following testing. Then, the low-velocity impact test will be implemented with varying initial velocities and impacting tubs to investigate the load-carrying capacity and the energy absorption of the CFRP plate during the impact. Also, the after-impact characteristics, like the fiber breakage, matrix damage, and delamination, will be studied. Finally, by using the X-ray micro-tomography as a non-destructive technique (NDT), the intra-laminar damages could be defined with their location, dimension, and also the damage evolution could be observed through the thickness direction.

In Chapter 4, the numerical method will be applied to simulate the LVI testing, and the results such as force, deformation, and energy absorption during the process will be compared with the experimental data from the LVI testing. Also, the model is defined with the 2D Hashin failure criteria to output the fringe to show different failure modes that develop during the impact. After the validation of the numerical modeling, the results

will also be compared experimentally and numerically by implementing different initial speeds and impactors. Since one important goal of this research is to develop the structure of the CFRP panel that becomes lighter to decrease the cost while maintaining the structural strength. So, the next Chapter is about sizing and shape optimizations of the CFRP plate that would give better damage resistance.

In Chapter 5, the first part is the size optimization, which aims to minimize the weight of the plate while satisfying the constraint requirement. With the same original model set up with the PCL code, the thickness and the ply orientation will be resigned. Besides, the possibility of using OpenMDAO for sizing optimization under nonlinear dynamic responses would be introduced. The second part is about shape optimization, based on the theory of shape basis vector will be performed, to minimize the weight, initial geometry of the plate is being improved. In this case, the constraints will be selected as displacement. In Chapter 6, the conclusion of this thesis will be given, recommendation and future work will be provided that could be continued and improved accuracy of LVI study. In this section, the research flow of Chapters 3-4 is shown in Figure 1.11 below.
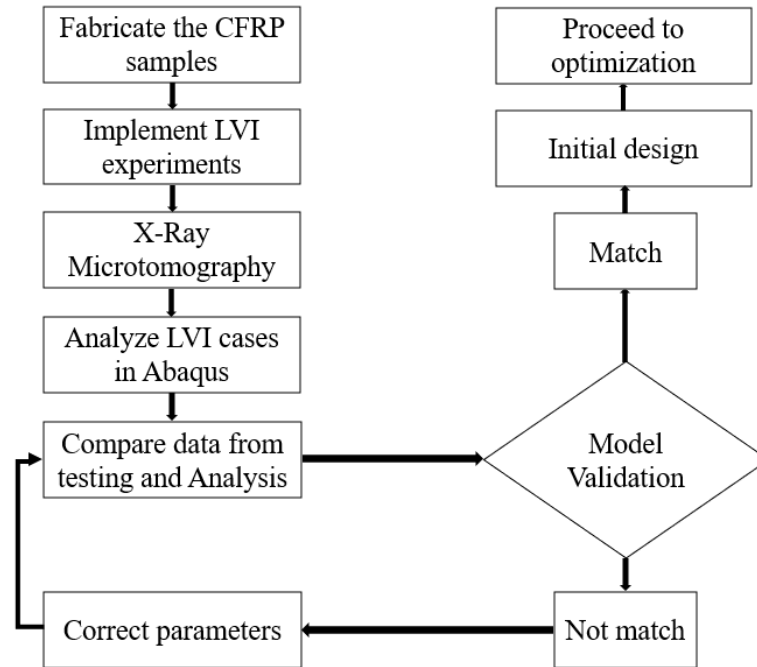
Figure 1.11 Flow process of numerical simulation.

2. Literature Review

From the early 1970s, low-velocity impact testing methodology was being used on composite materials. The Charpy, Izod, and Hounsfield methods that had been used on the metal materials were performed on the composite materials for impact investigation, and the researchers were utilizing the same testing equipment on composite structures. Those early attempts provided valuable experience for the testing techniques to keep getting progression in the past decades. The testing instruments were changed to be more suitable for composite testing and the according standards were created. Along with the formation of various failure theories of composite materials, the visible damage observed during the experiment could be explained and the damage could be even predicted before the impact testing. Later, these scientific research of LVI on composite would be helpful when applying to the real structure being utilized in the aerospace industry and other fields, and improved the structure design and evaluation in the fabrication, assembling, and maintenance process.

Although LVI testing could study the impact of damage on composite, it is often costly and time-consuming. Therefore, some novel methods of parametric studies were developed to solve this issue in a more rapid and also accurate way. Therefore, many researchers have been working on the modeling of the LVI, and the finite element analysis (FEA) is the most popular approach. Nowadays, the software packages provide the ability to impact analysis, the frequently used are ABAQUS, LS-DYNA, ANSYS, MSC.NASTRAN, etc. They help to understand the contact behavior of the composite and predict the possible damage progression. Also, when comparing the simulation results with the experimental data, they can get accurate agreement. However, some nonlinear

problems of FEA could lead to errors: the material and boundary nonlinearity, which relate to the failure criteria being used, the contact algorithm, and determination of time step for the LVI analysis.

Structural optimization is a comprehensive and active technology these days. Design optimization is to search for an optimal, or "the best" design, through changing the structural parameters. In this research, the redesigned parameters could be the ply thickness, ply orientation, or the geometric shape of the composite panel, and the redesign could give better impact resistance of the panel under LVI. While performing the search, the design is guided by the requirements on the responses of the plate, like the maximum displacement, peak contact force, and limits on the structural parameters. Such a design optimization task could be defined as the design concepts of "objective", "design variables", "design constraint", which will be included in the research.

2.1. Prior Research of LVI Experiment

Thomas (1973) used a drop-weight impact machine to test on the CFRP composite plates and the impact-resistance was quantified regarding Izod impact energy. With the adjustment of fiber volume and surface treatment of notching, it would result in the reduced impact strength. Also, most energy was absorbed in delamination. Due to the nonlinearity of impact with depth, calculation of results scaling should be performed.

Also Ross and Sierakowski (1973) offered the idea that the fiber orientation, mixing combination of filaments, and volume fracture would have a great effect on the impact resistance of the composite. The layup of the fiber was an important factor to determine the failure mechanisms and energy dissipation after impact.

From 1983 to 1984, a 16 layer CFRP laminate fabricated with UD ply or a mixing of UD and woven fabric was implemented LVI tests by Cantwell et al. (1983). The impacted samples were taken to do the fatigue tests. Two years later, they changed the fiber with another high-strain carbon fiber and conducted the tests again. Then, in 1989, Cantwell and Mortan tested on the circular CFRP composite plates and they determined the influence of sample shape on the penetration threshold parameter values.

In 1984, Caprino et al. (1984) found that the elastic modulus would not cause much effect in the impact, and the dynamic loading applied during impact, instead of the parameters of the impactor, is the dominant values that may change the results. Also, an energy-based equation was used to predict the elastically behavior when the failure happens under the impact. Then, Caprino et al. (1985) further expanded the work by using a simple energy-based model, enabled to predict the contact force during LVI between the impactor and plate. The predicted contact force-displacement history curve was well-matched with the experiments done using three different composite materials.

A large amount of prior research was about the LVI damage caused by relatively large mass objects. Later in the 1990s, Kumar and Rai (1993) studied the LVI damage on both of the CFRP and GFRP panels and emphasized the BVID caused by smaller mass impactors. The impact object was accelerated and released from a gas gun, and this setting could simulate the damage caused by runway stones to the aircraft. The apparatus of the gas gun is shown in Figure 2.1. The research was about the detection of delamination area by varying the depth of the interfaces. There, the shape and expanding direction of delamination were studied. Also, when using a higher impact energy with the

same impactor, there would be more delamination and even the damage would exist in all the layers.

In 1995, Pavier and Clarke (1995) compared the after-impact characteristics of a damaged specimen to the one with the imitated impact damage. By changing the mass of the impactor while keeping the shape the same, the impact energy could be adjusted.
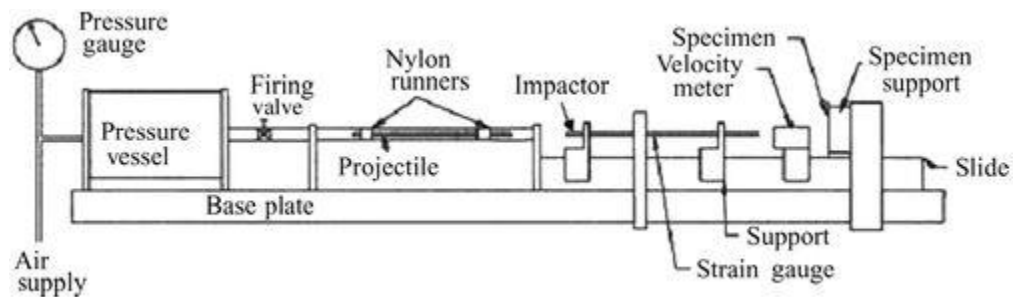
Figure 2.1 Apparatus of gas gun (Kumar & Rai, 1993).

The impact rig and plate fixtures are shown in Figure 2.2. With the X-radiography method, the strength reduction was measured under tension and compression. The experiment showed fiber crack was the main form of damage under tension that led to strength reduction, and the strength reduction under compression mainly due to the delaminated layers.

A great amount of research had handled with perpendicular impact on the composite, whereas not much was about the impact with an angle of inclination. In real cases, the oblique impact is much more common and therefore needs to be studied. Madjidi et al. (1996) further reported the damage tolerance of composite facing oblique impact force. By using the plate inclination between $30°$ and $50°$ with the interval of $5°$, the conclusion was that when the plate inclination increased, the residual tensile strength would increase.

Also, the normal impact force is more vital than the tangential impact force, which always causes greater gross damage to the plate. At last, for a certain impact energy level, direct impact would cause much more severe damage comparing to oblique impact.

2.2. Prior Research of LVI Finite Element Analysis

In real applications, the curved composite plate is more widely used than a flat plate. Leylek et al. (1999) represented a possibility of using finite element (FE) analysis to study the LVI on a curved composite plate. Compared with the testing results, the contact parameters were also obtained by running non-linear explicit FE in MSC.DYTRAN.
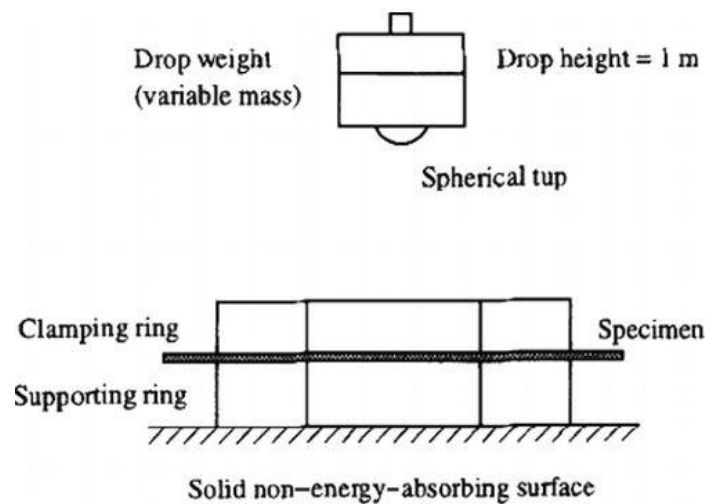
Figure 2.2 LVI setting up (Pavier & Clarke, 1995).

Since the response could be defined as a function regarding to impact velocity, mesh size, point of mass, and plate curvature, MSC.DYTRAN could perform the analysis rapidly and accurately. The results could also be utilized as guidelines for the experiment. The conclusion showed that the contact force will decrease until it comes to a constant value if the plate curvature increases. Also, the consideration of bending effects needs to be included when changing the low-velocity condition, and more studies need to be

continued. Besides, the determination of mesh size could bring uncertainties to the FE analysis, increasing mesh size would get higher impact energy values. However, simply decreasing the mesh size would not have much improvement on the results.

LS-DYNA is another popular nonlinear FE code, which uses explicit time integration to solve transient dynamic cases. Gower el at. (2007) used LS-DYNA to determine the dynamic response of a laminated Kevlar 29 and 129 composite panel, the plane wouldn't be penetrated after impact. It used MSC.PATRAN as pre-processor to set up the model. To achieve better accurate results, the element size in the impact zone was small and increase to a larger size until reaching the ends of the plate. The results were the impactor velocity-time curve, displacement-time curve, stress-strain curve, and impactor energy-time curve, both had good validation with experimental results.

Besides, the model successfully predicted the damage progress during the process. Except for the prediction of fiber damage and matrix cracking, the method of using a user-defined cohesive finite element could model delamination. The damage initiation and evolution are included with failure criteria. Here, Figure 2.3 shows the penetration process of the 9 mm hemispherical impactor colliding with the Kevlar 29 composite plate at 203 m/s. Only the quarter model was used. It was clear that at 0.00015 s, the impactor penetrated most of the plies, and left evident delamination damage among the penetrated plies. The damage simulation well matched with the real impacted panel. Unfortunately, the other damage types, like matrix crack, were not considered.
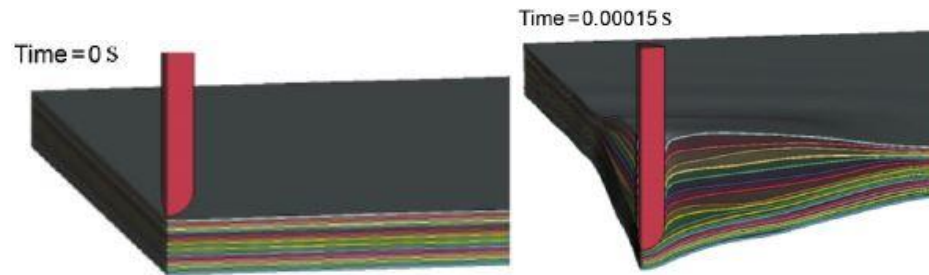
Figure 2.3 Quarter of the impact model (Gower et al., 2007).

As the progressive damage of composite happens at the microscale level, and the general impact (like the indentation on the surface) happens on the global level, it is necessary to apply a multiscale method to explore this complicated problem. However, when the displacement is too large, like the ballistic impact, unpredicted problems may arise (Talreja, 2006).

ABAQUS has also presented great possibilities for defining the impact analysis of composite in the ABAQUS/Explicit section. The user-defined material subroutine (VUMAT) includes the 2D/3D progressive damage theory and is used to simulate the LVI and analyze the residual strength values. The user could use several failure theories at once and compare the impact results from each of the theories. Moreover, the damage initiation and progression under LVI could be obtained. ABAQUS is also capable of modeling delamination with the method on the interface element to predict delamination and crack growth. This method accompanies the cohesive zone modeling (CZM) and virtual crack closure technique (VCCT), (Abir et al., 2017).

Liu et al. (2016) used ABAQUS to explore the effect of different failure criteria: Hashin criteria (Hashin & Rotem, 1973), Chang-Chang criteria (Chang & Chang, 1987), and Puck criteria (Puck & Schürmann, 2002) on the CFRP composite laminate. First, a sensitivity study was included in determining the density of mesh (refine the mesh until a

critical result). Then, the FEA results of contact force, max deflection, Von Mises stress

are verified with experimental results. Besides, the author analyzed the influence of the

shape of the impactors on displacement and stress. Also, the paper studied the material

and initial speed of the impactors (made from aluminum and steel) that may influence the

impact loading and displacement. The main damage types as matrix tension and

delamination were shown in the interface level responding to the fiber orientation in the

layers. Part of the results are shown in Figure 2.4.
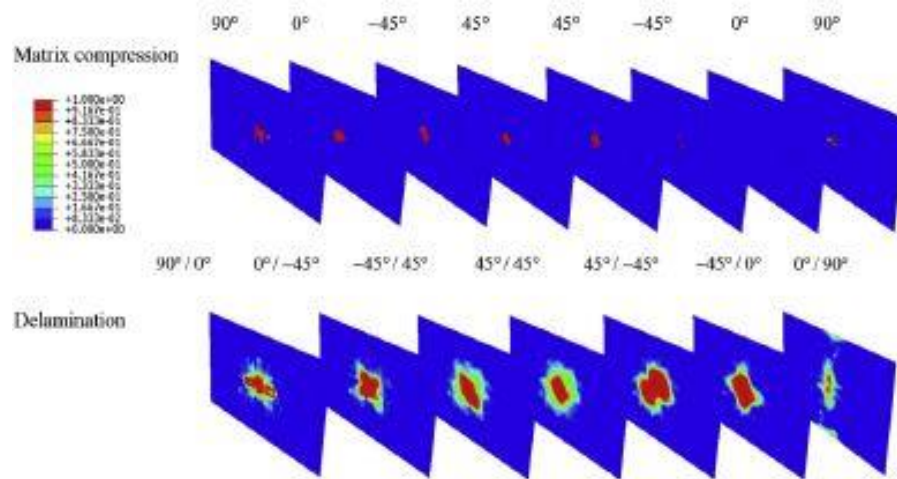
Figure 2.4 Matrix compression and delamination interface at 3.5ms with Hashin criteria (Liu et al., 2016).

2.3. Prior Research of Structural Optimization

A variety of optimization theories and algorism are applied for structural

optimization. As for the optimization methods, such as sizing, shape, and topology

optimization are the most classical ones, while topometry optimization is developed from

size optimization, and topography optimization is more like topology optimization. When

dealing with a structural redesign task, the complex problem could be solved by some

commonly used commercial software as MSC. Nastran, Genesis, and OptiStruct. The

available application fields of each software are provided in Figure 2.5. In this research,

the choice of using MSC. Nastran to solve size optimization and shape optimization is

based on its excellent ability to deal with sizing, shape, and topology optimization.

Furthermore, it is compatible with the off-the-shelf pre-processor software, MSC.

PATRAN, through patran command language (PCL). This combination could deal with

the finite element analysis and the optimization analysis, and post the design results as

fringe plots, animation, and curves, which is efficient.

	MSC Nastran	Genesis	OptiStruct
Linear static response optimization	O	O	O
Linear transient dynamic response optimization	O	X	X
Nonlinear static response optimization	O	O	O
Nonlinear transient dynamic response optimization	X	O	O
Fatigue response optimization	O	X	O
Linear buckling response optimization	O	O	O
Frequency response optimization	O	O	O
Multi-body dynamics optimization	X	X	O
Heat transfer optimization	X	O	O
Multiple model optimization	O	X	O
Global optimization	O	X	O
Super-element optimization	O	O	X
Parts-element optimization	O	O	X
Aero-elastic optimization	O	X	X

Figure 2.5 The application scope of different optimization software (Choi et al., 2016).

In 1960, the method of structural optimization was first brought up by Schmit

(Schmit, 1960) and was described mathematically. Generally, the optimization would

define one or several variables, the objective is to maximize or minimize the responses of

the structure, and the whole process should satisfy the design constraint as well. Later,

the optimization was gradually employed by FEM and the optimization software that

used FEM. To express the optimization task in a quantitative form, a typical linear

optimization statement could be expressed as follows (MSC Nastran user's guide design

sensitivity and optimization, 2017): Find X to minimize/maximize

$$F(X) \quad \text{objective} \tag{1}$$

$$g_j(X) \leq 0 \quad j = 1, \ldots, n_g \quad \text{inequality constraints} \tag{2}$$

$$h_k(X) = 0 \quad k = 1, \ldots, n_h \quad \text{equality constraints} \tag{3}$$

$$x_i^L \leq x_i \leq x_i^U \quad i = 1, \ldots, n \quad \text{side constraints} \tag{4}$$

$$X = \{x_1, x_2, \ldots, x_n\} \quad \text{design variables} \tag{5}$$

The nonlinear programming (NLP) method is applied in gradient-based optimization

problems, and it comprises the direct method and approximation method. The MSC.

NASTRAN uses NLP in both size and shape optimizations. The direct method allows the

algorism fully in charge of the optimization. In an approximate method, the design

functions are approximated to the explicit function of the variables, and NLP control the

modified functions.

For instance, the optimization algorisms could be feasible directions (MMFD),

sequential quadratic programming (SQP), and sequential linear programming (SLP).

MMFD is used when the optimization starts in the feasible region and remains feasible

during the design. For SQP, the starting point could be either infeasible or feasible, and

could efficiently handle equality constraints (Choi et al., 2016). In MSC. NASTRAN, it

uses the MSCADS and IPOPT optimizers. According to the MSC Nastran Design

Sensitivity and Optimization User's Guide, when using MSC Nastran SOL 200, the

program automatically uses MSCADS for size optimization and IPOPT for topology

optimization. The MSCADS algorithms are adapted from the public domain versions of ADS codes (Arora, 2012). Besides, the IPOPT algorithm is a special purpose optimization algorithm to address design tasks with a large number (> 3000 to 4000) of design variables and has its primary application to topology optimization tasks, but can be applied to the conventional design tasks that are discussed in this document as well.

The IPOPT algorithm implements an interior point line search filter method. The DOT and BIGDOT algorithms from Vanderplaats R&D Inc. are not available in Nastran 2010 and subsequent releases. However, the DOT and BIGDOT algorithms can be found in earlier releases. In this part, a flow chart of the methodology is shown in Figure 2.6, which helps to summarize all the steps take to finish the optimization in MSC. NASTRAN. Then, the detailed description of the primary functions is explained below in this figure (MSC Nastran user's guide design sensitivity and optimization, 2017).

The purpose of constraint screening is to limit the number of constraints for the redesign that considers whether they'll play an active role in the redesign. For example, when the current values of the normalized constraints exceed the "Truncation Threshold" that is denoted by TRS, the ones that below this threshold would be temporarily deleted to help decrease the difficulty of the optimization design task.
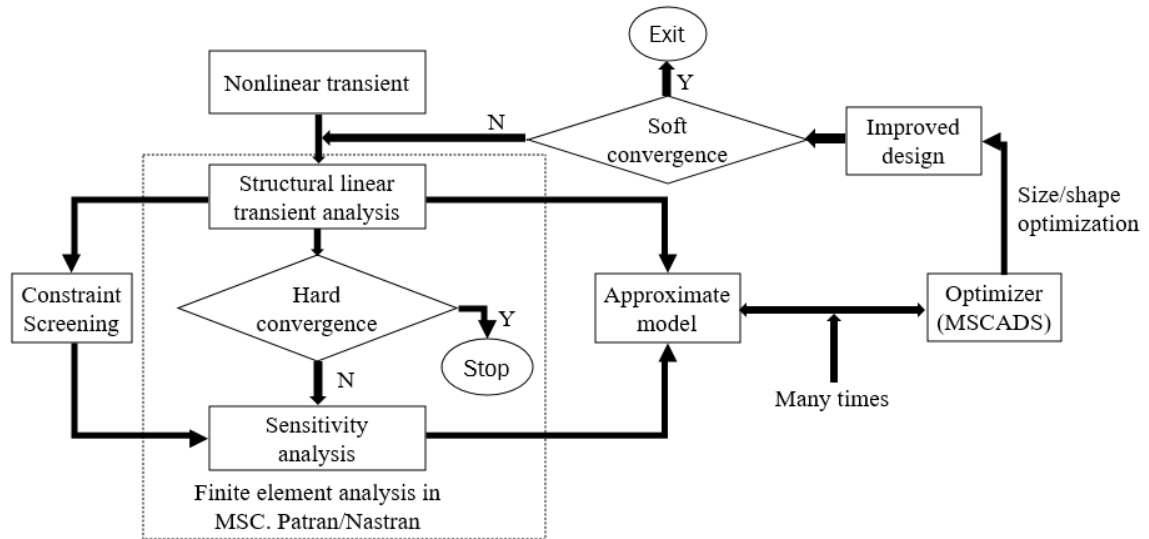
Figure 2.6 Flow process of structural optimization (MSC Nastran user's guide design sensitivity and optimization, 2017).

Design sensitivity analysis shows the changing rate of the response quantities corresponding to the changes in the design variables. The sensitivity analysis is performed automatically before the optimization that provides the useful information of the gradients. Therefore, it avoids the high cost of repeating during optimization. Besides, it is also used for parametric study with the sensitivity information rather than implementing the optimization. To be noted that, the sensitivity is for the responses used in the objective and constraints. For example, it could use the direct and adjoint sensitivity techniques, and Finite element methods.

The approximate model associates with the optimizer to provide the required information, such information exchange would continue many times. The model provides the information of function values (The values of objective and constraints) and gradient values (The values of gradients of the objective and constraints to the design variables). By applying a method like the Taylor Series expansion, the finite element analysis will be approximated to a region where is locally valid.

There are two types of convergence, soft convergence, and hard convergence. Soft convergence compares the output results from the approximate optimization with the inputs, if the variables changed greatly, the updated response will start the new design cycle. Normally, the soft convergence won't stop the whole program and it will only terminate the design cycle instead. Hard convergence compares the results of the finite element analysis which are based on the previous design cycles, if the convergence is satisfied, the whole optimization process would stop and the locally optimized design is achieved.

During each design cycle, the values of the constraints would be represented by using its normalized values, which saves much computational time. Here, the satisfied constraint would be negative.

2.4. Mode-Independent Failure Theory

The strength of the CFRP laminates relies on the stacking sequence of the laminae, and therefore the fiber orientation in the laminae is an important factor. The classical laminate theory (CLT) is basing on the stacking sequence and material properties and could obtain the stress and strain results in the layers. Also, CLT is based on the hypothesis that it is a thin, perfectly adhered laminate, in which the laminae is made from orthotropic materials.

Thus, the mode-independent theories, such as the Tsai-Wu theory, Tsai-Hill, and Hoffman, are being used to predict the damage lamina failure in the stress and strain space. The lamina stresses would be translated into the local axes on the laminae, and theories would make the judgment based on the shear strength and normal strength of the laminae. However, the model is linearly elastic and doesn't include the progressive

damage of composites. Thus, it couldn't distinguish different failure modes, like fiber or matrix failure. The most simple mode-independent failure theories are the maximum strain and maximum stress criteria. Only one stress or strain component is included in each of the theories. Thus, these two theories are also known as "non-interactive criteria" because the only component of stress or strain would interact with the criteria. For instance, longitudinal tension is not connected with the transverse shear.

In this research, the Tsai-Wu failure theory (Tsai & Wu, 1971) is chosen as the quadratic failure criteria for progressive failure analysis. Although there are different forms of Tsai-Wu theory, this study used Equation 6 to calculate the failure index in the plane stress state:

$$F_1\sigma_1 + F_{11}\sigma_1^2 + F_2\sigma_2 + F_{22}\sigma_2^2 + F_{66}\tau_{12}^2 + F_{12}\sigma_1\sigma_2 = FI \tag{6}$$

$$F_1 = \frac{1}{X_T} - \frac{1}{X_c} \quad F_{11} = \frac{1}{X_T X_c} \quad F_2 = \frac{1}{Y_T} - \frac{1}{Y_c} \quad F_{22} = \frac{1}{Y_T Y_c} \quad F_{66} = \frac{1}{S^2} \tag{7}$$

$$F_{12} = -\frac{1}{2}\frac{1}{\sqrt{X_T X_C Y_T Y_C}} \tag{8}$$

Where in Equation 6, FI is the failure index, "1" and "2" denotes the longitudinal and transverse directions, respectively. In Equation 7-8, "X" and "Y" indicates the allowable strength in the fiber and transverse directions, respectively. Also, "T" is tensile strength, while "C" is compressive strength. At last, "S" is the in-plane shear strength.

2.5. Mode-Dependent Failure Theory

Mode-dependent failure theories could define the particular failure modes depending on the theories used. During the past decades, Hashin criteria (Hashin & Rotem, 1973), Chang-Chang criteria (Chang & Chang, 1987), and Puck criteria (Puck & Schürmann,

2002) are the often-used ones for LVI damage simulation. Hashin proposed the theory that considered four different damage initiation mechanisms: fiber tension, fiber compression, matrix tension, and matrix compression, which are expressed in the effective stress space.

Hashin criterion requires that the behavior of the material is linearly elastic with small elastic strain when it is undamaged. Likewise, Chang-Chang's criteria is basing on the longitudinal and transverse tension and compression of the fiber and matrix damage. After Hashin, Puck and Schürmann added the missing part in Hashin's theory, they explained the orientation of the inclined fracture plane, and it helped to determine the inter-fiber fracture from the fiber fracture. Also, this theory of fracture plane is based on the transverse compression of matrix shear strength. Figure 2.7 shows the fracture plane by reference to the material coordinate, and Equation 9 defines the Puck's criterion for compressive damage mode (Shi, 2014).
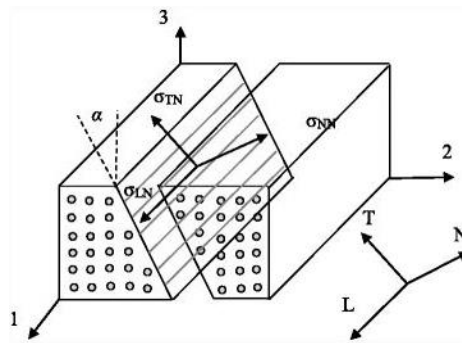
Figure 2.7 Fracture plane of matrix compressive damage (Shi, 2014).

$$F_{mc} = \left(\frac{\sigma_{NT}}{S_{23}^A + \mu_{NT}\sigma_{NN}}\right)^2 + \left(\frac{\sigma_{NL}}{S_{12} + \mu_{NL}\sigma_{NN}}\right)^2 = 1 \qquad (9)$$

Where $\sigma_{ij}(i, j = L, T, N)$ are the stresses $\sigma_{ij}(i, j = 1,2,3)$ rotated to the fracture plane, relative to the material coordinate system. Although Puck's theory is able to include the fracture plane, the accuracy needs to be improved. Also, it is not clear whether defining the fracture plane angle could allow damage simulation to be more realistic under dynamic loading. Although Puck criteria show some advantages over Chang-Chang and Hashin, Puck needs more material properties to implement. However, the CFRP laminates tested in this research is lack of such material information, the material supplier didn't provide enough properties. Besides, Hashin is available in the FE software ABAQUS, and the material properties satisfy the requirements. Considering the cost and numerical precision, Hashin criteria are chosen in this study. In ABAQUS, Hashin failure criteria has already been adopted, without the need of using VUMAT.

The Hashin criteria, combining the damage initiation criteria with the energy dissipation-based damage evolution method, can predict damage propagation. A detailed description of the damage theory will be introduced in Chapter 4.

3. Experimental Approach

In this Chapter, several experiments were designed to explore the after-impact characteristic and impact damage of the selected CFRP composite plate. The 10-layer cross-ply laminates were fabricated using the hot press machine in the Embry-Riddle lab. Then, LVI tests were done with two different impactors, the output data from the impact instrument helped to study the factors, such as displacement, contact force, impact energy, and the shape of the impactors, which may affect the damage tolerance of the plate. After that, the X-ray imaging technique was implemented to get the radiographs that showed the existing failure modes among the layers of the plate with BVID.

3.1. Fabrication of the CFRP Composite Plate

The CFRP prepreg material used was the UD carbon fiber/3900 series epoxy prepreg from HEATCON Composite Company (Tukwila, WA), the detailed material data sheet is in Appendix A. The prepreg was stored under 10 °F (-12.22 ℃) during the transportation to ensure the life span of the material, and it was kept frozen before fabrication. The CFRP samples were fabricated with 10 layers, and each was trimmed to get the dimension of 4in x 6 in (101.6 mm x 152.4 mm) with the Leco MSX255 Benchtop (St. Joseph, MI) Sectioning Machine illustrated in Figure 3.1 (a). During layup, the fiber filament was arranged in a 0/90 cross-ply configuration, with the layers stacked in order.

The CFRP samples were fabricated in a Wabash Compression Press (Wabash, IN), which is shown in Figure 3.1 (b). Two aluminum mold plates were used at the bottom and upper platform of the machine to give a uniform pressure on the laminate, and the excessive epoxy on the plate was cleared by acetone after the curing. Then, the bagging film was applied on top of the aluminum plate, it would be in direct contact with the peel

ply, and it helps to remove the laminates from the aluminum plate after curing, without leaving the excessive epoxy on it. Also, it could withstand the high temperature and creates a smooth surface on the laminate. After that, the peel ply from FiberGlast Corporation (Brookville, OH) was placed above the film, the function of the Nylon peel ply fabric in the curing is two-fold. As pressure loading consolidates the laminate, the squeezed-out epoxy goes through in the composite layer and is absorbed by the breather fabric. Because of its open structure, air flows easily through the breather fabric allowing the air to be evacuated from the consolidated laminate. Next, the stacked laminated is placed, and another set of peel ply and releasing film would be applied above the laminated. At last, the aluminum foil and the upper aluminum plate were used on top of the releasing film to help removing the laminates after curing. The laminates layup is demonstrated in Figure 3.2.

A continuous loading of 2 Ton (19,613 N) was implemented by the Wabash Compression Press, and the laminates would be cured for 120 min at 350 $^{\circ}$F (177 $^{\circ}$C) according to the curing cycle requirements. Before finishing the process, the laminates would be cooled with the hydraulic and air cooling system to room temperature. After removing the plate from the machine, the excessive epoxy on the edge was trimmed with the sectioning machine to get the size of 4 in x 6 in (101.6 mm x 152.4 mm). The composite plate after fabrication is shown in Figure 3.3.

3.2. Low-Velocity Impact Testing

For the impact test under LVI, the drop-test was realized by following the specification on the ASTM D7136/D7136M (American Society for Testing and Materials, West Conshohocken, PA) impact test standards and using a drop-tower. The

drop-tower used was the Instron (Norwood, MA) 9250 HV Impact Test Instrument,

shown in Figure 3.4 (a).

(a)   (b)
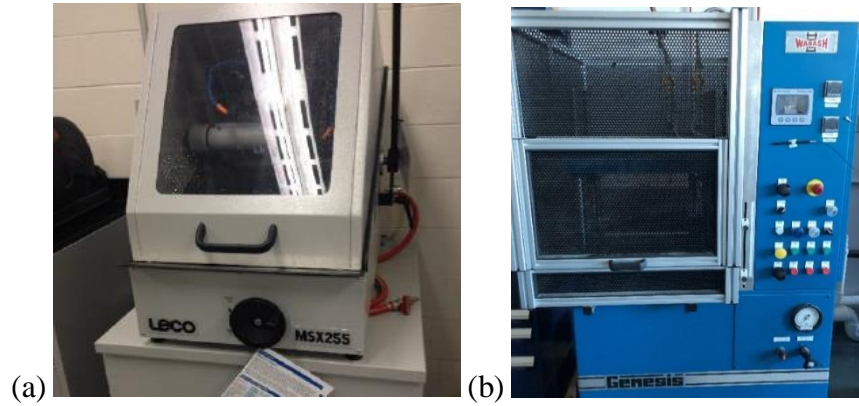
Figure 3.1 a) Leco MSX255 Benchtop Sectioning Machine, and b) Wabash Compression Press.

(a)   (b)
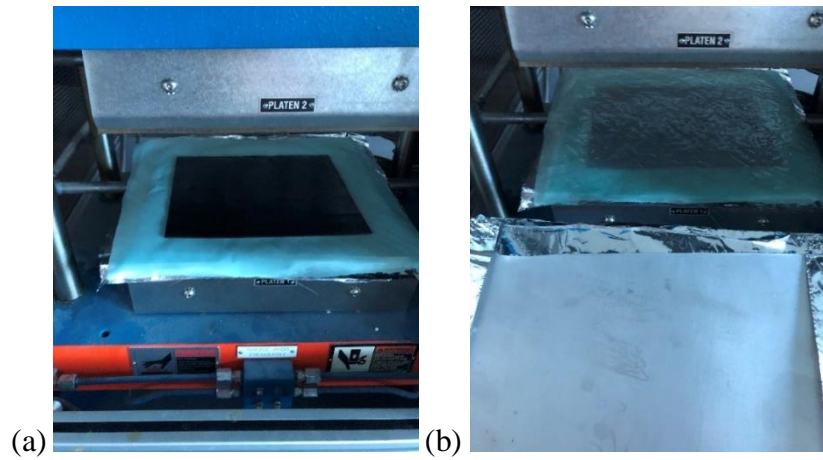
Figure 3.2 a) Half of the layup, and b) final layup .

Figure 3.3 Trimmed composite samples for LVI testing (total is 6).

In the testing, two types of steel impactors were used, which were the 15.88 mm hemispherical steel indenter and the 20 mm cylindrical indenter based on the shape of tips, and they are shown in Figure 3.4 (b). Also, there were amounted with adjustable crosshead and drop weights, a pneumatic clamp, rebound brake, a load cell instrumented equipped above the impactors, and the Impulse DAQ system and Controller - Version: 3.6.76 which helped to output various impact response values. An impact mass of 6.69 kg was used for the hemispherical steel indenter and the mass of the cylindrical indenter was 6.63 kg. Then, the impact speeds of 1.0 m/s, 1.5 m/s, and 2.0 m/s were implemented on 3 samples with the hemispheric impactor. Considering the penetrating abilities of the impactors, the cylindrical impactor used higher impact speeds. Therefore, the impact speeds of 2.0 m/s, 2.5 m/s, and 3.0 m/s were performed on the rest of the 3 samples with the cylindrical impactor.

In Figure 3.5, it demonstrates the setup of the drop-tower in detail. The clamp fixture fixed the four edges of the test specimen(s). These fixed boundary conditions were provided by a pneumatic clamping device which applied an 85-psi shop air (was used) to clamp the sample. The rebound brakes were adjusted to the proper height by using washers and spacers, this step helped to avoid any second impacts (only one impact event would happen). Before actual testing, the velocity indicator helped to set the initial impact speed.

Also, some spare composite plates were used to define the proper impact speed that could give the wanted damage result, and they helped to measure the force range needed in the DAQ system. During testing, the Impulse DAQ system and Controller were used to output the data. The sensor used was the load cell that recorded the contact force. By

using the differential relation, the values of acceleration, displacement, and energy could

be obtained. For instance, the acceleration of the load cell could be calculated by dividing

the contact force by the mass of the impactors.

(a) (b)
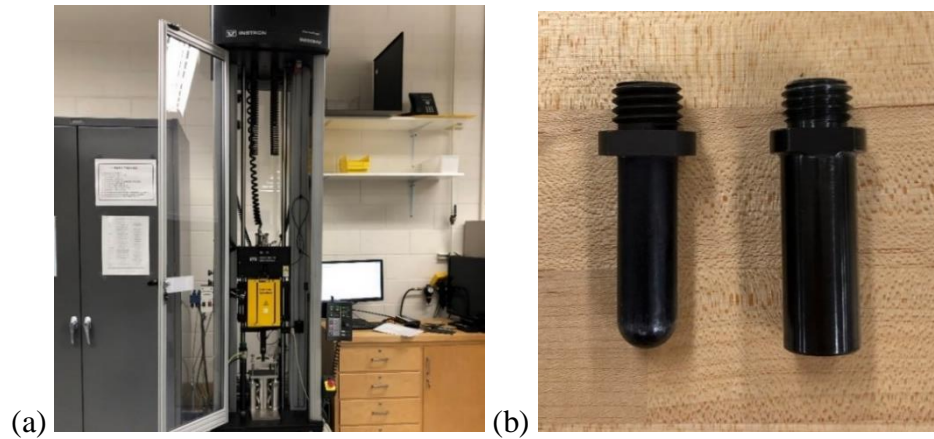
Figure 3.4 a) Instron 9250 HV Impact Test Instrument, and b) two impactors.
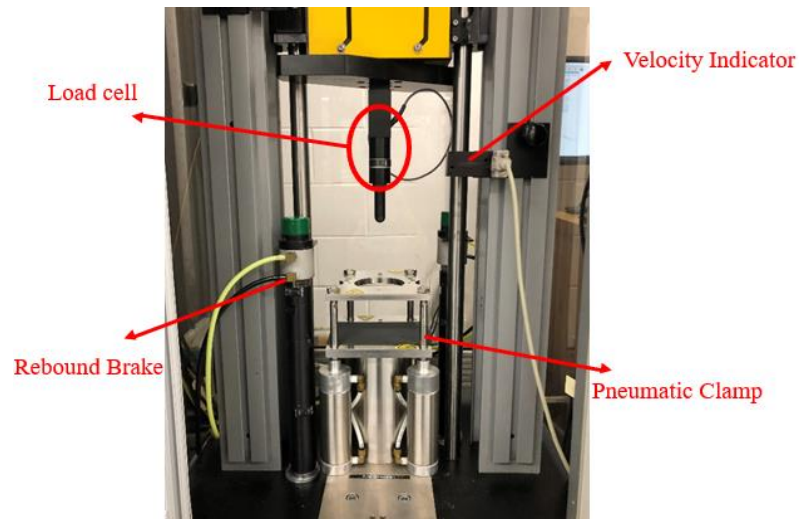
Figure 3.5 Component parts of the drop-tower.

A numerical integration method was used, the acceleration would help to get the velocity and displacement in the impact. As for the impact energy, when the impactor with mass m impacts the plate with velocity v_0, the energy of the impactor becomes E_i.

$$v_i(t) = v_0 - \frac{1}{m} \int_0^t F_{exp} dt \tag{10}$$

$$E_i = \frac{mv_0^2}{2} \tag{11}$$

$$KE(t) = \frac{mv_0^2}{2} - \frac{m\left(v_i(t)\right)^2}{2} = E_e + E_a \tag{12}$$

Where the contact force F_{exp} is obtained from the load cell. Besides, the kinetic energy KE (t) is divided into the elastic energy E_e and the absorbed energy E_a. The elastic energy is also called rebounding energy. The absorbed energy is the same as "releasing energy", which happens when the damages initiate and release a certain amount of energy, and it would be absorbed by the plate rather than converting into elastic energy. Such damages could be intra-laminar failure and/or inter-laminar damage, the quantity of the absorbed energy depends on the amount of the failures. As for the actual kinetic energy, around 5% of energy loss was dissipated into other forms, such as friction, vibration of the plate, heat dissipation, and damage. After the LVI tests, the impacted samples are shown below.

In Figure 3.6 (a), it is seen that the hemispheric impactors caused a white and pitted indentation in the impacted area for all three samples. This phenomenon was produced by the localized contact stress developed by the hemispheric tip. On the backside of the

plates illustrated in Figure 3.6 (b), only the one impacted at 2 m/s showed BVID as fiber

splitting, and it was then chosen for damage detection using the X-Ray micro-

tomography method. However, the cases of 1 m/s and 1.5 m/s didn't have any visible

damage. As for the impacted plates with cylindrical impactor, there were circular areas

that defined the contact region on the front side, which is demonstrated in Figure 3.7 (a).

(a)

(b)
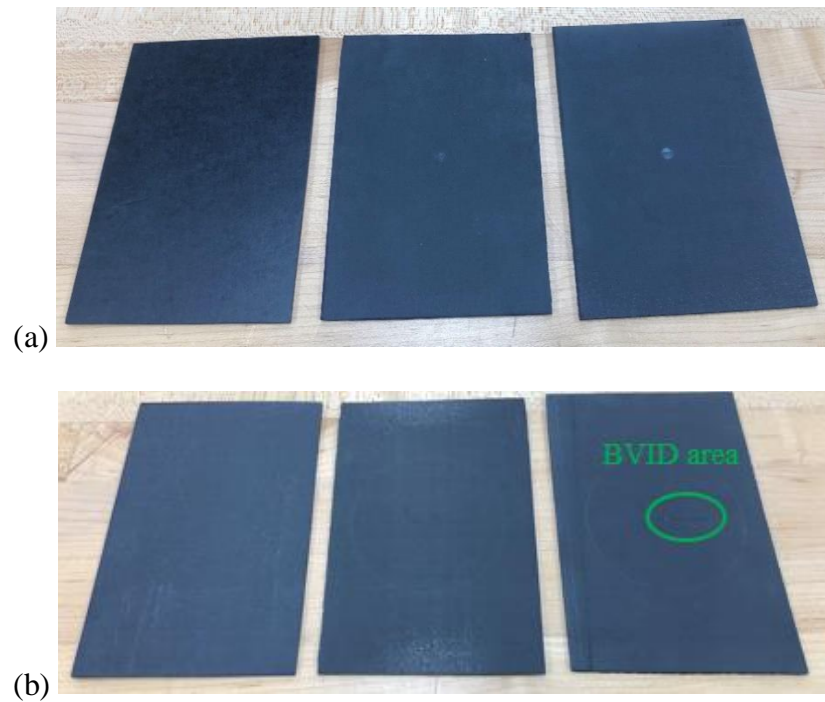
Figure 3.6 Impacted plates with hemispheric tip impactor, a) front side, and b) backside, from left to the right: 1 m/s, 1.5 m/s, and 2 m/s.

(a)

(b)

Figure 3.7 Impacted plates with cylindrical impactor, a) front side, and b) backside, from left to the right: 2.0 m/s, 2.5 m/s, 3.0 m/s.

Because of the bluntness of the cylindrical tip, no obvious indentation was observed on the front side. On the back side shown in Figure 3.7 (b), no visible damage was detected for the three samples. It could be indicated that the impact speed didn't have adequate momentum to penetrate the plies and leave the fiber damage on the un-impacted side. To make the contents more concise, the impact characteristics such as displacement, contact force, and impact energy, etc. would be presented in Chapter 4 and compared with the simulation results.

3.3. X-Ray Microtomography

Abrate (Abrate, 1998) announced that the non-destructive damage evaluation (NDE) method could be used to study the failure mechanisms of composite structure under impact. Whereas, the destructive evaluation is capable of providing more detailed information. The combination of both NDE and destructive methods is the better way that improves the accuracy. In this research, to have a more detailed observation of the internal damage of the impacted laminates, an NDE method: X-Ray radiology, was applied.

This method provides a feasible way to detect and distinguish any damage modes like fiber damage, matrix damage, and delamination. Also, by scanning through the laminate in different directions, a 3D structure of the plate is obtained, and it helps to measure the actual location and size of the damage inside the samples. The X-ray imaging device used was the Skyscan X-Ray Microtomography machine (Bruker Corporation, Billerica, Massachusetts), shown in Figure 3.8.

Since there was a requirement on the dimension of the samples, the maximum height should below 120 mm and the width should be less than 96 mm. However, the task was to focus on the damaged area that was much smaller than the maximum size constraints. Thus, the sample impacted with hemispheric impactor at 2 m/s was selected to detect the intra-laminar damages. It was trimmed into a smaller size that kept the impacted area at the center region. Also, this procedure expedited the scanning process on a smaller sample. Thus, the size of the samples became 4 cm $\times$ 6.5 cm for scanning.

During scanning, the sample rotated around on a fixture, and hundreds of pictures were created in omni-direction. Since the composite material would absorb much radiant energy, a low voltage energy of 15 kv, 150 μA was chosen, and it gives better penetration and resolution of the x-ray. Then, the scanning pictures helped to form the 3D image of the sample in the CTVOX software through the reconstruction process. From the result, it showed fiber crack and matrix damage among the laminates, and delamination was not recognized. In Figure 3.9 below, it was created by sectioning the sample in the X-Y, X-Z, and Y-Z direction to produce a 3D configuration of the sample. Besides, with the specified scale in Figure 3.10, the length, width, and depth of crack propagation in the

direction of thickness could be measured. To validate the damage model in ABAQUS,

only the damages on the top and bottom layers were detected for comparison.

Figure 3.8 Skyscan X-Ray Microtomography (15 kv, 150 µA).
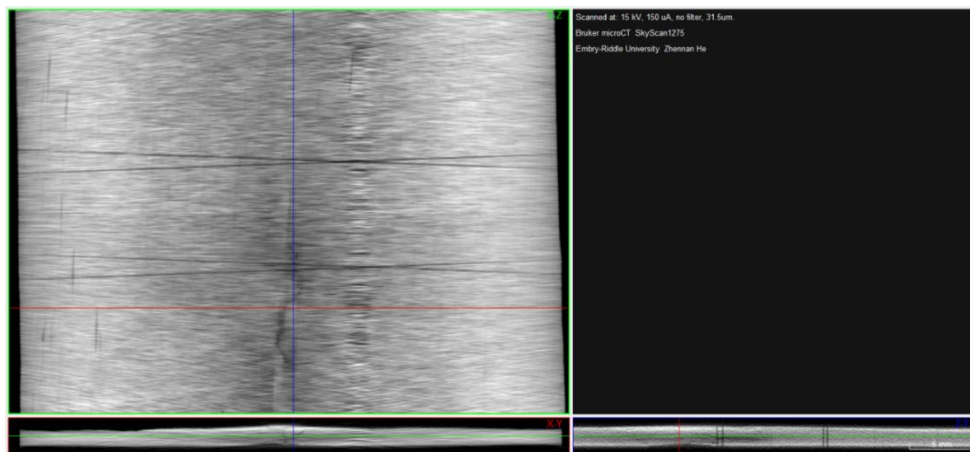
Figure 3.9 Intra-laminar damage after image reconstruction.

In Figure 3.10 (a), the circular impact indentation area was around 2.45 mm^2. The

size of the fiber damage on the top layer was 3.8 mm $\times$ 0.4 mm (1.52 mm^2), observing

from Figure 3.10 (b). From Figure 3.10 (c), the fiber damage area in the horizontal

direction of the bottom layer was approximate to be 20 mm $\times$ 2.5 mm (50 mm^2). To be

noted that the two intersecting and parallel lines in both Figure 3.9 and Figure 3.10 could

be caused by the resolution issues of the x-ray scanning. Because of the low radiation

voltage used, the resolution was relatively decreased.

(a)

(b)

(c)
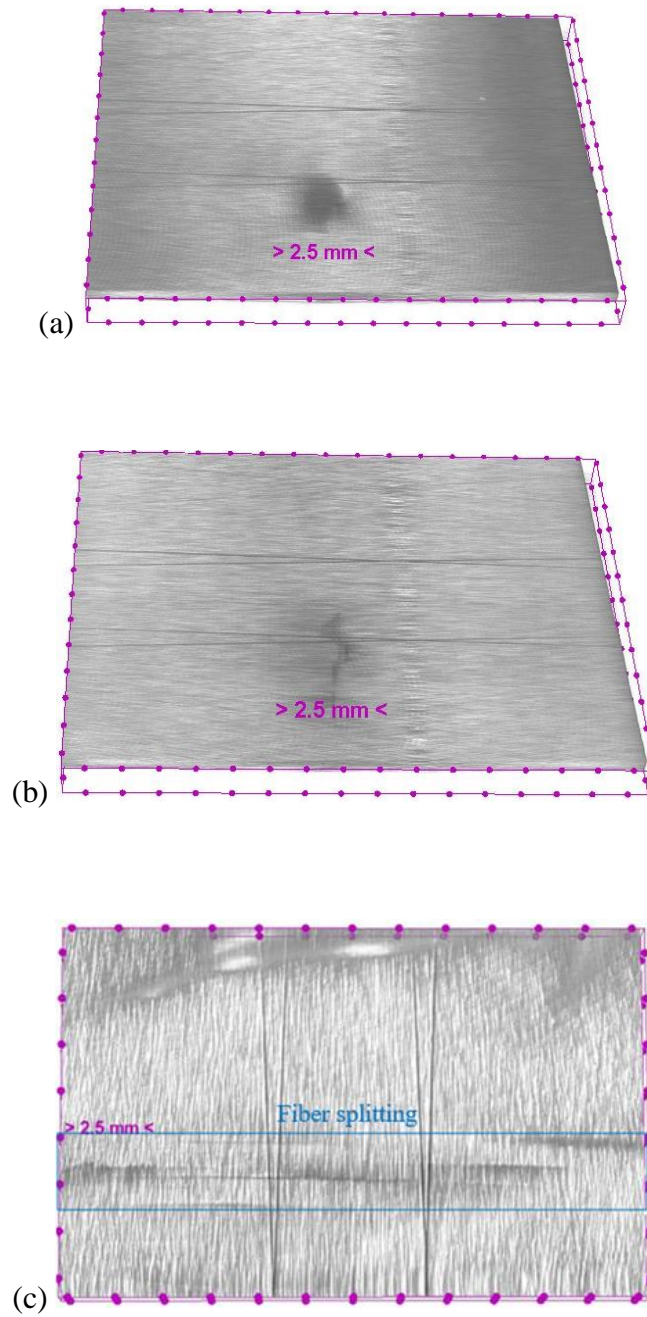
Figure 3.10 a) Indentation on the impacted side, and the fiber splitting damage on the b) top (impacted) layer, and c) bottom (unimpacted) layer.

4. Numerical Simulation

In this Chapter, the emphasis was to validate the experimental results from Chapter 3 with the numerical model used in ABAQUS. Based on the low-velocity impact, the same nonlinear dynamic loading was used in the model. The output would be displacement, contact force, energy absorption, and the curves obtained from these values were corresponding to the curves from the DAQ system in the LVI testing. Also, the Hashin failure criteria was applied to verify the damage results with the X-Ray radiology results. Since the value of the shear modulus G_{23} was missing from the material information sheet in Appendix A, an estimation method was introduced to approximate the value. Besides, the intra-laminar failure model used in ABAQUS would be described.

4.1. Estimation of the Shear Modulus

Here, the value of the shear modulus G_{23} is not provided by the manufacturer, so it needs to be estimated based on proper theories. For instance, the semi-empirical Halpin-Tsai model is used to predict the stiffness of fiber-reinforced composites with great fiber alignment (Hull & Clyne, 1996). Also, it is widely used to predict the properties of the reinforced composite materials with short fibers. Equation 13 is to calculate the shear modulus G_{23},

$$G_{23} = \frac{E_2}{2(1 + v_{23})} \tag{13}$$

Where the Poissions ratio,

$$v_{23} = 1 - v_{12} - \frac{E_2}{3K} \tag{14}$$

K is the bulk modulus of the composite, and it is expressed as:

$$\left[\frac{f}{K_f} + \frac{(1-f)}{K_m}\right]^{-1} \tag{15}$$

$$\text{With } K_f = \frac{E_f}{3(1-2v_f)} \text{ and } K_m = \frac{E_m}{3(1-2v_m)} \tag{16}$$

Where E_2 is the elastic modulus in the transverse direction, f is the volume fraction of the fiber, E_f and E_m are the fiber and matrixes young's modulus, v_m and v_f are the matrices and fiber's volume fraction. Whereas, it requires the parameters of the composite constituents (v_m, v_f, E_m, E_f), which are not provided by the manufacturer. Kuo et al. (2007) developed one method that could estimate the mechanical properties of the lamina (v_{23}, G_{23}) by using the Wave Equations and the criteria for UD orthotropic material. Also, this present method agreed well with the data provided by other publications.

In this part, the classical laminate theory (CLT) for the lamina would be shown, the derivation and calculation of the stiffness matrix Q would be done, and the wave equations would be used combining with the expression of the Q matrix to get the v_{23}, then use the relation between the G_{23} and v_{23} to get the value of G_{23}. However, two restrictions need to be satisfied, (a) the lamina should be unidirectional material which shows transverse isotropic properties in the 2-3 plane, (b) the fiber in the cross-section must be uniform in the 2-3 plane. The stress and strain relation of an orthotropic lamina is shown in the following equations.

$$[\sigma] = \begin{bmatrix} \sigma_{11} \\ \sigma_{22} \\ \sigma_{33} \\ \sigma_{23} \\ \sigma_{31} \\ \sigma_{12} \end{bmatrix} = \begin{bmatrix} Q_{11} & Q_{12} & Q_{13} & 0 & 0 & 0 \\ Q_{12} & Q_{22} & Q_{23} & 0 & 0 & 0 \\ Q_{13} & Q_{23} & Q_{33} & 0 & 0 & 0 \\ 0 & 0 & 0 & Q_{44} & 0 & 0 \\ 0 & 0 & 0 & 0 & Q_{55} & 0 \\ 0 & 0 & 0 & 0 & 0 & Q_{66} \end{bmatrix} \begin{bmatrix} \varepsilon_{11} \\ \varepsilon_{22} \\ \varepsilon_{33} \\ \gamma_{23} \\ \gamma_{31} \\ \gamma_{12} \end{bmatrix} \tag{17}$$

And
$$\begin{bmatrix} Q_{11} = E_{11} \frac{1-v_{23}v_{32}}{\Delta}, & Q_{12} = E_{11} \frac{v_{21}+v_{31}v_{23}}{\Delta}, & Q_{13} = E_{11} \frac{v_{31}+v_{21}v_{32}}{\Delta}, \\ Q_{22} = E_{22} \frac{1-v_{13}v_{31}}{\Delta}, & Q_{23} = E_{22} \frac{v_{32}+v_{12}v_{31}}{\Delta}, & Q_{33} = E_{33} \frac{1-v_{12}v_{21}}{\Delta}, \\ Q_{44} = G_{23}, & Q_{55} = G_{13}, & Q_{66} = G_{12}, \end{bmatrix} \tag{18}$$

$$\Delta = 1 - v_{12}v_{21} - v_{23}v_{32} - v_{13}v_{31} - 2v_{21}v_{32}v_{13}$$

Here, three Young's modulus (E_{11}, E_{22}, and E_{33}), three shear modulus (G_{12}, G_{13}, and G_{23}), and three Poisson's ratios (v_{12}, v_{13}, and v_{23}) are specified in Equations 17-18. Also, the dynamic inertial force is included, and the motion could be expressed by the density ρ, displacement u_i, and time t:

$$\frac{\partial \sigma_{1i}}{\partial x_1} + \frac{\partial \sigma_{2i}}{\partial x_2} + \frac{\partial \sigma_{3i}}{\partial x_3} = \rho \frac{\partial^2 u_i}{\partial t^2} \quad i = 1,2,3 \tag{19}$$

Here, considering the normal stress and shear stress that affect the displacement, the scalar ϕ and vector ψ, which denotes the compression and shear waves, replace the component in Equation 19 to get the wave expressions in Equations 21-23 based on Equation 20:

$$u = \nabla\phi + \nabla\psi \tag{20}$$

$$(Q_{12} - Q_{13} + Q_{66} - Q_{55}) \frac{\partial^3 \psi_1}{\partial x_1 \partial x_2 \partial x_3} = 0 \tag{21}$$

$$(Q_{23} - Q_{12} + Q_{44} - Q_{66}) \frac{\partial^3 \psi_2}{\partial x_1 \partial x_2 \partial x_3} = 0 \tag{22}$$

$$(Q_{13} - Q_{23} + Q_{55} - Q_{44}) \frac{\partial^3 \psi_3}{\partial x_1 \partial x_2 \partial x_3} = 0 \tag{23}$$

If further split Equations 21-23 and substitute the expression of the components of the Q matrix, four equations could be obtained, and they include one compression wave equation and three shear wave equations. The solution of the wave equation is described in Equation 24, and R is the wave amplitude, ω is angular frequency, and k is the wavenumbers in the principal direction. In Equations 21-23, the results can be shown in Equation 25 since $\partial^3 \psi_3 / x_1 \partial x_2 \partial x_3 \neq 0$.

$$\psi_i = R \cdot \exp(j[\omega t - k_1 x_1 - k_2 x_2 - k_3 x_3]) \tag{24}$$

$$Q_{23} - Q_{12} + Q_{44} - Q_{66} = Q_{13} - Q_{23} + Q_{55} - Q_{44} \tag{25}$$

Since $Q_{12} = Q_{13}, Q_{55} = Q_{66}$, replacing the value of $E_{11}, E_{22} = E_{33}, G_{12} = G_{13}, v_{12} = v_{13}$, the unknown values of v_{23} and G_{23} become:

$$v_{23} = \frac{-E_{22}\left[E_{11}\left(\frac{1}{2} - v_{12}\right) + 2G_{12}v_{12}{}^2\right] + \Delta}{2E_{11}G_{12}} \tag{26}$$

$$G_{23} = \frac{E_{22}}{2(1+v_{23})} \tag{27}$$

Where the expression of Δ is:

$$\sqrt{E_{22}{}^2[E_{11}(0.5 - v_{12}) + 2G_{12}v_{12}{}^2]^2 - 4E_{11}G_{12}[E_{11}E_{22}(0.5 - v_{12}) - G_{12}(E_{11} - 2E_{22}v_{12}{}^2)]}$$

The material properties of the CFRP composite plate are shown in Table 4.1, and the values are found in Appendix A. By inputting these values into Equations 26-27, the estimated value of G_{23} is about 2.54 GPa.

Table 4.1

Mechanical properties of the T800S carbon/3900 Epoxy lamina under 22°C

Properties	Value
ρ/(kg/m^3)	1580
E_1/(GPa)	148
E_2, E_3/(GPa)	8.3
ν_{12}	0.33
G_{12}/(GPa)	3.93
X_T/(MPa)	2965
X_c/(MPa)	1779
Y_T/(MPa)	60.3
Y_c/(MPa)	214
S_T, S_c/(MPa)	68.9

4.2. Intra-Laminar Damage Model

By using some analytical failure models in the finite element method (FEM), the constitutive behavior of the composite material could be studied. The accuracy of the damage analysis largely depends on the model used. Nowadays, lots of researches have implemented continuum damage mechanics (CDM) to discover the behavior of composite laminates. The Hashin failure criteria is one of the theories that successfully help to predict the damage initiation. In the ABAQUS material library, the 2D Hashin failure criteria are used for the continuum shell element. If the structure is modeled in a 3D solid element, the 3D Hashin failure criteria is capable under the out-of-plane loading condition. Then, the prediction of the damage evolution process could be achieved with

the energy-based law, which was proposed by Lapczyk and Hurtado (2007). Meanwhile, all the fracture energies values need to be defined depending on the failure modes.

As mentioned in Chapter 1, the main damage forms of thin laminate made from thin lamina are fiber splitting and matrix damage. Also, this phenomenon was verified in the X-Ray micro-motograph testing. Thus, the focus on the after-impact failure study should be on the intra-laminar damage of the impacted plate. As the property of laminates will be modeled with shell elements, and the "through-the-thickness" stress distribution is unimportant for the thin plate, the progressive failure criteria used is the 2D Hashin criteria, and the damage initiation equations are shown in Equations 28-31.

$$\text{Fiber tension } (\hat{\sigma}_{11} \geq 0) \quad F^t{}_f = \left(\frac{\hat{\sigma}_{11}}{X^T}\right) + \alpha\left(\frac{\hat{\tau}_{12}}{S^L}\right)^2 \tag{28}$$

$$\text{Fiber compression } (\hat{\sigma}_{11} < 0) \quad F^c{}_f = \left(\frac{\hat{\sigma}_{11}}{X^C}\right)^2 \tag{29}$$

$$\text{Matrix tension } (\hat{\sigma}_{22} \geq 0) \quad F^t{}_m = \left(\frac{\hat{\sigma}_{22}}{Y^T}\right)^2 + \left(\frac{\hat{\tau}_{12}}{S^L}\right)^2 \tag{30}$$

$$\text{Matrix compression } (\hat{\sigma}_{22} < 0) \quad F^c{}_m = \left(\frac{\hat{\sigma}_{22}}{2S^T}\right)^2 + \left[\left(\frac{Y^C}{2S^L}\right)^2 - 1\right]\frac{\hat{\sigma}_{22}}{Y^C} + \left(\frac{\hat{\tau}_{12}}{S^L}\right)^2 \tag{31}$$

In Equations 28-31, X^T is longitudinal tensile strength, X^C is longitudinal compressive strength, Y^T is transverse tensile strength, Y^C is transverse compressive strength, S^T is transverse shear strength, and S^L is longitudinal shear strength. Where α is a coefficient that defines the contribution of shear stress to the fiber tensile initiation criterion, in the model Hashin used, α was set to 1. The $\hat{\sigma}_{11}$, $\hat{\sigma}_{22}$, $\hat{\tau}_{12}$ are the components of effective stress tensor $\hat{\sigma}$, and

$$\hat{\sigma} = M\sigma \tag{32}$$

Where σ is the normal stress, and M is the damage matrix:

$$M = \begin{bmatrix} \dfrac{1}{(1-d_f)} & 0 & 0 \\ 0 & \dfrac{1}{(1-d_m)} & 0 \\ 0 & 0 & \dfrac{1}{(1-d_s)} \end{bmatrix} \tag{33}$$

Where d_f, d_m, d_s are damage variables of fiber, matrix, and shear, their values are based on tension/compression, and the values are:

$$d_f = d^t{}_f \; if \; \hat{\sigma}_{11} \geq 0 \; or \; d_f = d^c{}_f \; if \; \hat{\sigma}_{11} < 0 \tag{34}$$

$$d_m = d^t{}_m \; if \; \hat{\sigma}_{22} \geq 0 \; or \; d_m = d^c{}_m \; if \; \hat{\sigma}_{22} < 0 \tag{35}$$

$$d_m = d^t{}_m \; if \; \hat{\sigma}_{22} \geq 0 \; or \; d_m = d^c{}_m \; if \; \hat{\sigma}_{22} < 0 \tag{36}$$

When a certain damage initiates, the damage evolution follows because of the degraded stiffness of the composite materials, and such reduction is based on the damage variables, varying from 0 (undamaged) to 1 (damaged). Also, the damage propagation is controlled by the values fracture energy dissipation, G_c. After damage initiation, the stiffness becomes:

$$\sigma = C_d \varepsilon \tag{37}$$

Where ε is the strain value, and C_d is the damaged elasticity matrix:

$$C_d = \frac{1}{D} \begin{bmatrix} (1-d_f)E_1 & (1-d_f)(1-d_m)v_{21}E_1 & 0 \\ (1-d_f)(1-d_m)v_{12}E_2 & (1-d_m)E_2 & 0 \\ 0 & 0 & (1-d_f) \end{bmatrix} \tag{38}$$

Where D$= 1 - \left(1 - d_f\right)\left(1 - d_m\right)\nu_{12}\nu_{21}$. Then, the damage variable for a certain

mode becomes:

$$d = \frac{\delta^f_{eq}(\delta_{eq} - \delta^0_{eq})}{\delta_{eq}(\delta^f_{eq} - \delta^0_{eq})} \tag{39}$$

Where δ^0_{eq} is the initial equivalent displacement when a failure mode initiates, δ^f_{eq}

is the displacement when full damage of that mode happens. Note that the design

variables in Equation 39 are controlled by the equivalent displacement, which could be

expressed by the stress components from Equations 28-30. Also, δ^f_{eq} depends on the

value of G_c regarding to each failure mode. However, the fracture energy may not be

feasible to measure through testing, thus, the values in Table 4.2 are based on

assumptions.

Table 4.2

Fracture energies of the CFRP composite samples

Properties	G^t_1/(N/mm)	G^c_1/(N/mm)	G^t_2/(N/mm)	G^c_2/(N/mm)
Value	45	45	7	7

4.3. LVI Modelling

The FE model was built in the pre-processor ABAQUS/Explicit module. To replicate

the same setting in the LVI testing, the geometry and weight of the composite plate and

the impactors are the same, and they have used 2D continuum shell elements and 3D

solid elements, respectively. The models of using different impactors could be found in

Figure 4.1. Also, Figure 4.2 shows the ply thickness is 1.9 mm and the 10-layer cross-ply

configuration. The size of the plate was 4 in x 6 in (101.6 mm x 152.4 mm). To improve

the accuracy, the circular impact region was using a denser mesh size (2.5 mm), and it could be modified later if needed.

The impactors were modeled as rigid bodies that could only move in the Z-axis during the impactor, and such motion relation was controlled by using the multi-point constraints (MPCs) on the centroid point in the impactors. As for the boundary condition, the fixed area is not allowed to move in both translational and rotational directions, which reflected the real LVI test setting. The initial speed of the impactors was corresponding to the value used in the LVI testing. Thus, 6 simulation tasks were implemented according to the two impactors and the impact speeds.

Besides, the enhanced reduced integration hourglass control and distortion control were defined. Also, the degradation law was applied on the plies, when the damage variable in the longitudinal direction exceeds 0.99 and the shear strain exceeds 1, the element would be deleted, it helped to reduce distortion and simulate the progressive penetration of the impactor. The contact property between the tip of the impactor and the impact surface of the plate was used as general contact, which speeded up the contact analysis. The friction coefficient between the impactor and the plate was 0.3. The time-stepping was set to 0.05 ms with a total of 10 ms impact time. When the LVI simulation job was completed, it took about 1 CPU hours on Intel Core i5-8660 @ 3.40 GHz with 8 GB RAM.

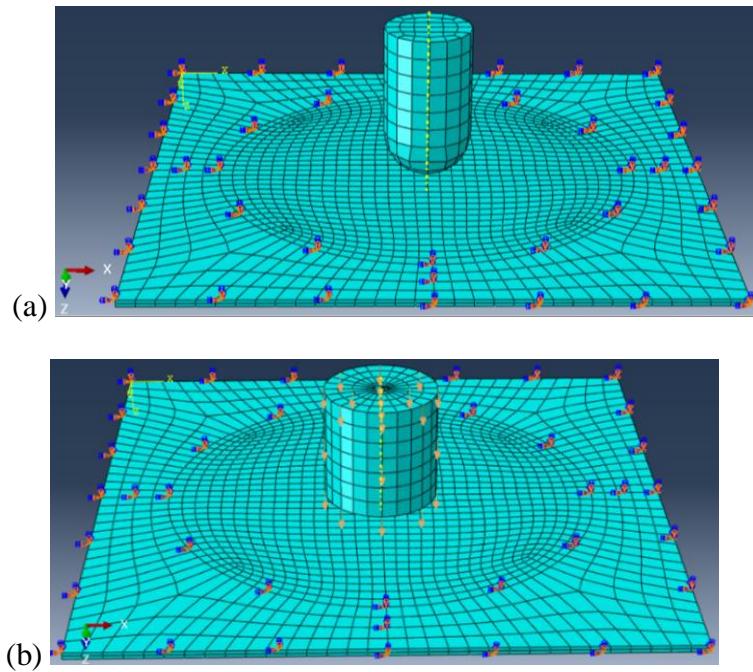*Figure 4.1* LVI models a) with hemispheric impactor, b) with cylindrical impactor.
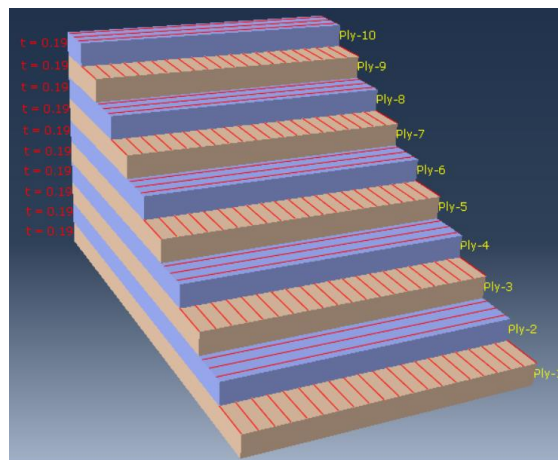

Figure 4.2 CFRP laminates layup.

4.4. Mesh Sensitivity Study

This part is to determine the best mesh size that balances the computational time but also gives accurate results. Generally, a denser mesh would lead to increasing peak force and would be more computationally costly. Here, the selection of peak force was to

verify the accuracy of the simulation, and CPU time is to balance the computational cost while maintaining the accuracy. Besides the peak force, deflection, and energy from different LVI cases could also be considered to determine the mesh size. The prime requirement was that the numerical results should match with the experimental results. Then, making a small adjustment of the mesh size should give relatively low computational time.

The case of the laminates impacted by the hemispheric impactor at 2 m/s was used to determine the proper mesh size. From the testing, the maximum contact force was 4.62 KN at 4.00 ms, and this value is marked in "green" in Figure 4.3. In the same graph, it is seen that curve of peak force increases rapidly and the CPU time would decrease greatly when using a mesh size less than 2.4 mm. Also, using the 2.4 mm mesh would produce a maximum value of 4.45 KN at 5.34 ms, which is close to the actual testing result. Besides, the 2.4 mm mesh size is more accurate than using the adjacent 2.2 mm mesh and 2.6 mm mesh. Moreover, the CPU time for analysis utilizing 2.4 mm mesh is at the lower range of the corresponding curve, which means it is way less computationally expensive than using a denser mesh.

After comparing the contact force results, the 2.4 mm mesh was also tested for the other response types. These responses results would be demonstrated in the following Subsections, which proves the accuracy of choose this mesh size.
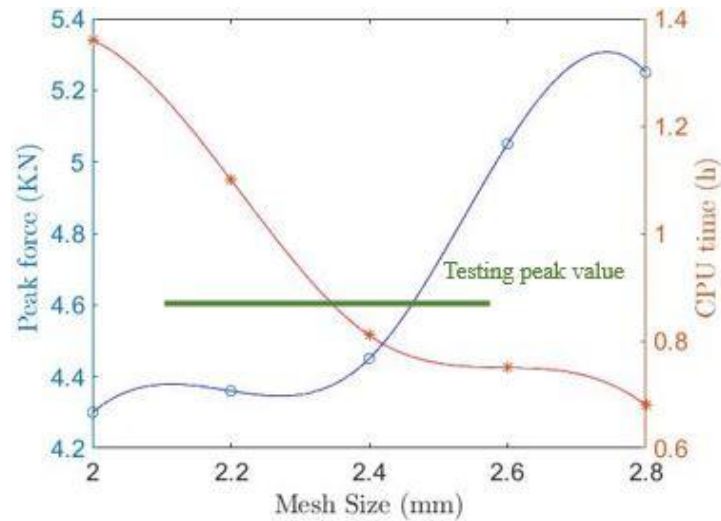
Figure 4.3 Peak contact force and CPU time with varying mesh size.

4.5. Validation of the LVI Numerical Simulation and LVI Testing

In this section, the after-impact characteristics from the LVI numerical simulation and

the testing would be compared based on the plots of contact force-time history,

displacement-time history, and impact energy-time history. The validation would be

implemented on the cases using hemispheric impactor and cylindrical impactor, and the

effect of the tip shape of the impactors would be discussed.

4.5.1. Results Comparison of Hemispheric Impactor

In this part, the structural response values are compared regarding varying initial

velocities through the numerical and experimental methods. Generally, the plots of the

impact process could be separated into two stages: the impacting stage from the start

point till the curve reaches its peak point and the bounding stage which is from the peak

to the ending. In Figure 4.4 (a), the three contact forces curves from testing indicate that

the increasing impact velocity (energy) would give greater contact forces, and both of the

cases reach the peak force values at around 4.5 ms. Also, the impact durations of the

three are similar, both are ended at around 9.2 ms. Although the curves are smooth, the

top parts of the 1.5 m/s and 2 m/s cases have minor oscillations, which manifest the possible crack was developing during these periods.

Besides, the oscillations of the load drops in the simulation results are more obvious than the testing results, which could be due to the overprediction of the fiber damages and matrix damages. Also, it takes a longer time for the curves to reach their peak value and finish the whole process. Moreover, the simulations are producing a relatively smaller maximum contact force value. However, the trends of the curves of the simulation model and the experimental results are very similar, and they are validated with each other even though with some acceptable differences.

(a)
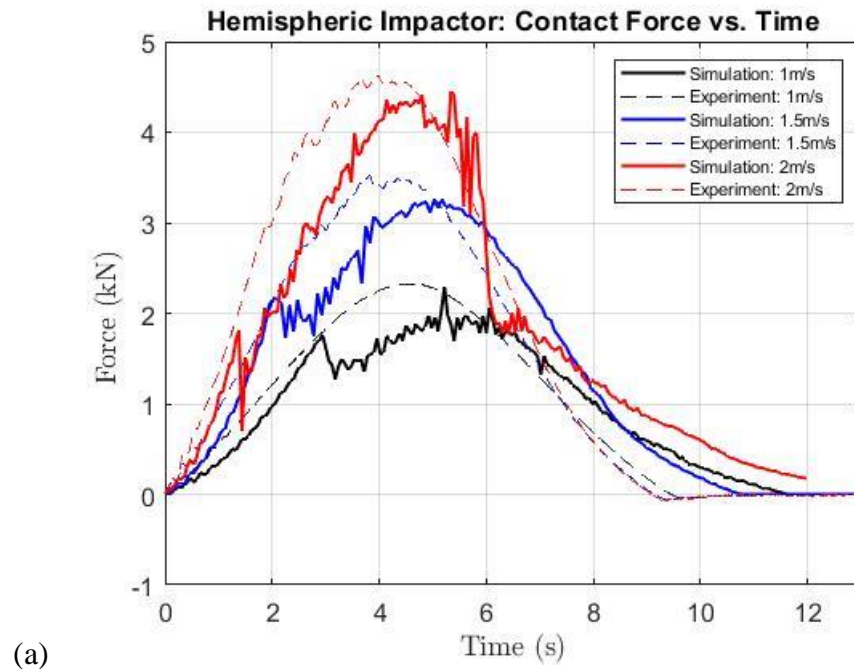
From Figure 4.4 (b), it is seen that the results from ABAQUS and testing are matched well, the impact duration times are close to 15 ms. Also, the delay in reaching the peak displacement in the simulation results is already proved in Figure 4.4 (a).

Hemispheric Impactor: Displacement vs. Time

(b)
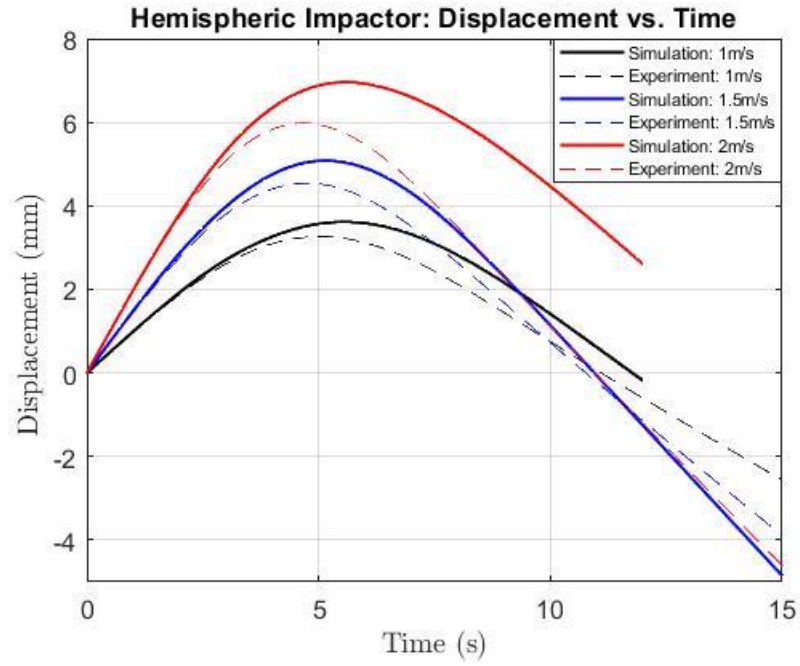
In Figure 4.4 (c), the 1 m/s case shows better agreement with the experimental results when comparing the other higher velocity cases. Whereas, the energy levels of the ABAQUS simulation are lower than the testing. There, the elastic energy E_e and the absorbed energy E_a are shown on the curve of the 1.5 m/s case. These two energy values with the minor energy loss values add up to the complete kinetic energy.
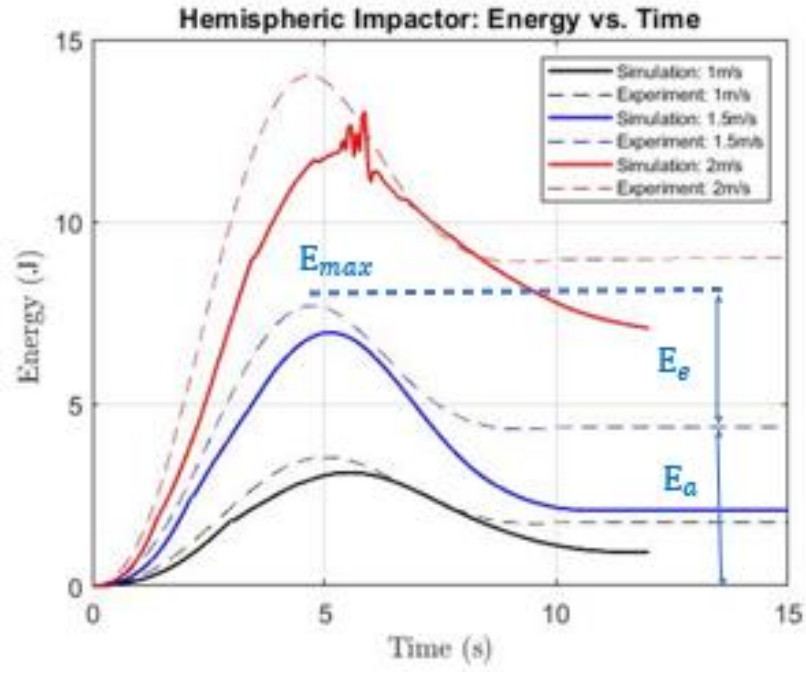
(c)

Figure 4.4 Impact response results of a) force-time history, b) displacement-time history, and c) energy-time history using hemispheric impactor.

4.5.2. Results Comparison of Cylindrical Impactor

Comparing the simulation using hemispheric impactor and cylindrical impactor, the results of the latter have better matches with the experiment, and are shown in Figure 4.5.

In Figure 4.5 (a), the three smooth curves from the testing indicate there weren't any detectable damages. While the curves form the simulation, especially for the 3 m/s case, shows evident ups and downs that may have failures. The elastic vibrations at the beginning could be explained by the friction between the plate and impactor, or it may because of the matrix damage initiation. Except for the above small differences, the simulations are quite close to each other.

(a)
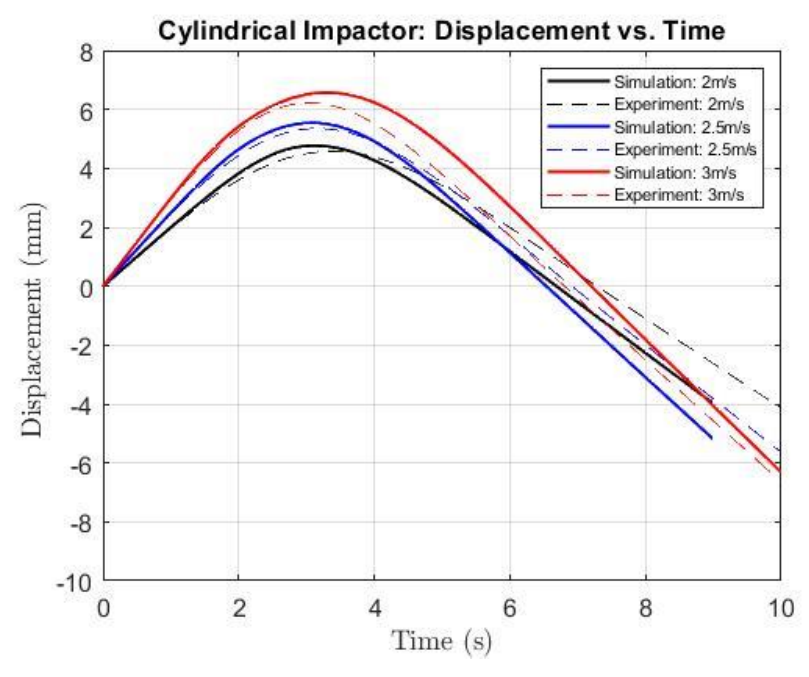
(b)

In Figure 4.5 (b) and Figure 4.5 (c), the success of the simulation is apparent, the

results are closer to the ones of using hemispheric impactor in Figure 4.4 (b) - (c). They

explain that a higher impact speed will result in increasing indentation and energy
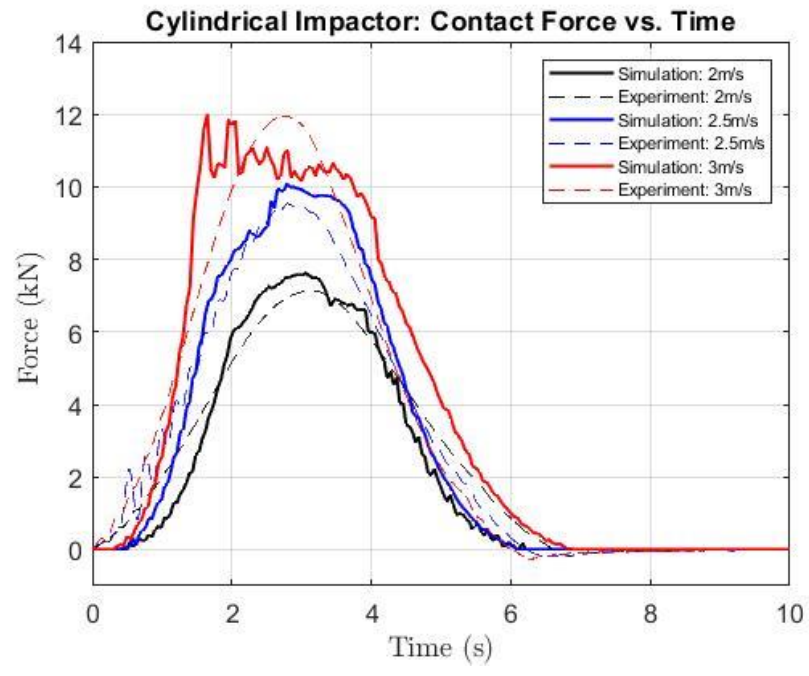
absorption.

(c)
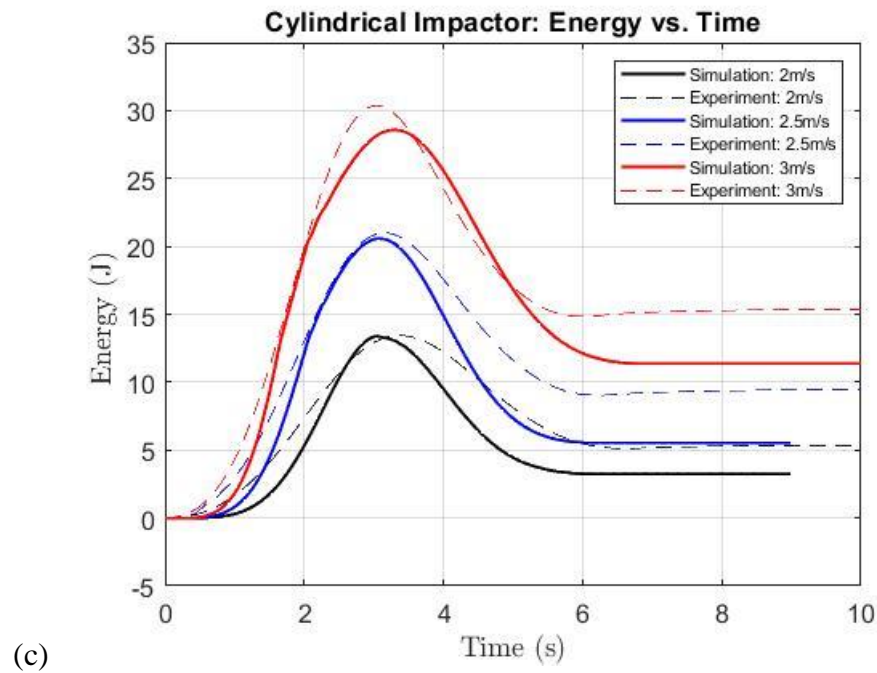
Figure 4.5 Impact response results of a) force-time history, b) displacement-time history, and c) energy-time history using cylindrical impactor.

Besides, the shape effect of the impactors are studied in Figure 4.6. Since the

impactors have similar mass, the shape of their tip becomes an important factor that

determines the structural responses. The cylindrical impactor's tip has a larger diameter

and thus possesses more bluntness, and leads to a much higher contact force. For the

hemispheric impactor with a smaller diameter, it brings more serious damages, and larger

deformation because of the localized forces.
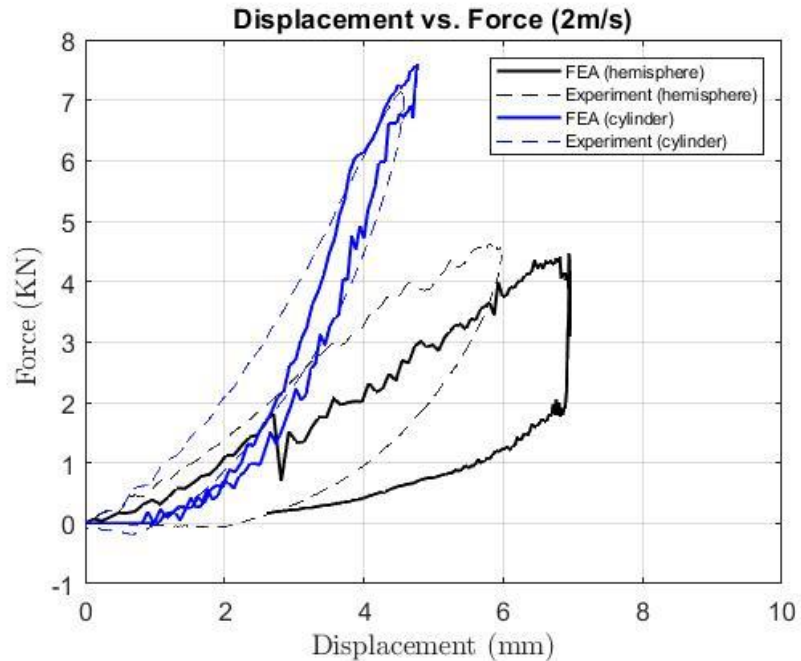
Figure 4.6 Force-displacement history of the impactors at 2 m/s.

4.6. Damage Results

In ABAQUS, the tensile/compressive fiber and matrix damages on the front side and backside of the plate were studied because these failure modes are the main failure modes that happened in the impact area. Also, the process of damages initiation and development can be presented in animations.

Here, the plate impacted at 2 m/s with the hemispheric impactor was studied for its possible impact damages. In addition, since the mesh size is defined in the LVI modeling, the dimension of the damaged area could be calculated. Therefore, this value should match the actual size of the impacted damaged area determined by the X-Ray imaging test.

Figure 4.7 (a) shows that the tensile fiber damage first initiates at the 1.56 ms of the ply on the impacted surface, and the completed damage area is shown in Figure 4.7 (b).

The size of the fiber damage is around 4.8 cm × 2.4 mm, which is similar to the one

obtained after X-Ray imaging. Then, the crack propagated through all the plies, which

created the fiber splitting at the backside of the plate.

(a)

(b)
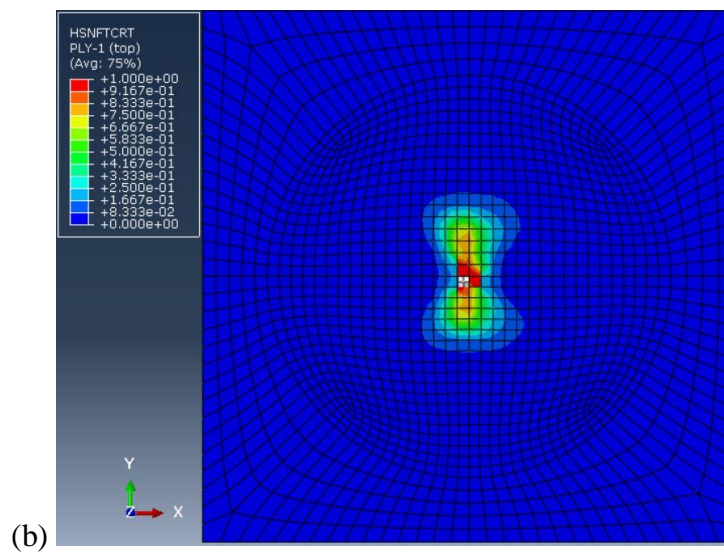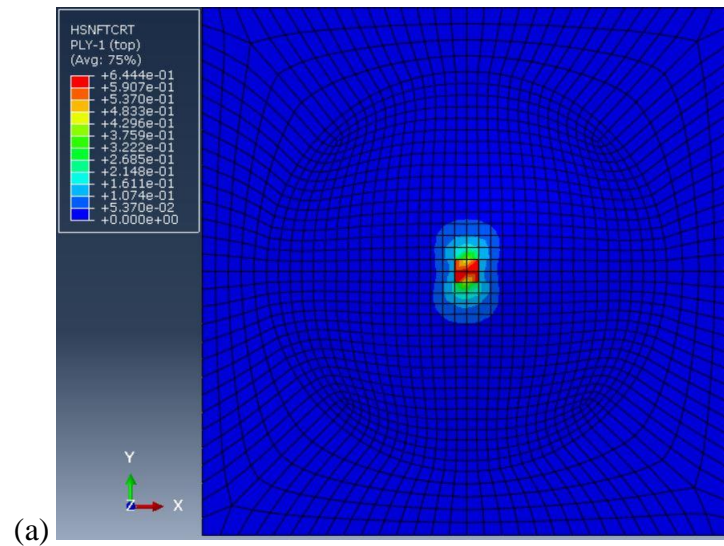
At 1.86 ms, the tensile fiber damage starts at the bottom layer, which is shown in

Figure 4.7 (c). At last, the length of the tensile fiber damage on the back in Figure 4.7 (d)

is 19.2 mm in the fiber direction, with a width of 2.4 mm, which creates a 46.08 mm^2

damaged area. As observed after the LVI testing and during the X-Ray imaging testing, the actual crack length was 20.0 mm, and the damaged area was observed as 50 mm^2. Thus, there's a good matching between the prediction and testing with a 7.84% difference, which is acceptable. The error could be due to the mesh size being used and the imperfect prediction of fracture energy selected for the failure modes.

(c)

(d)
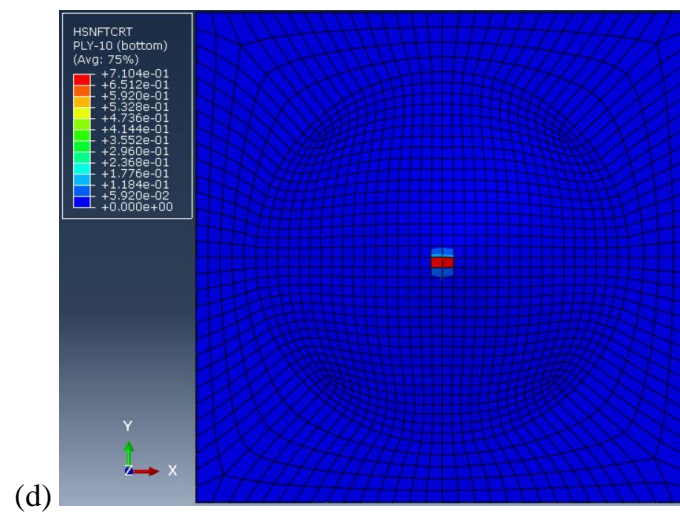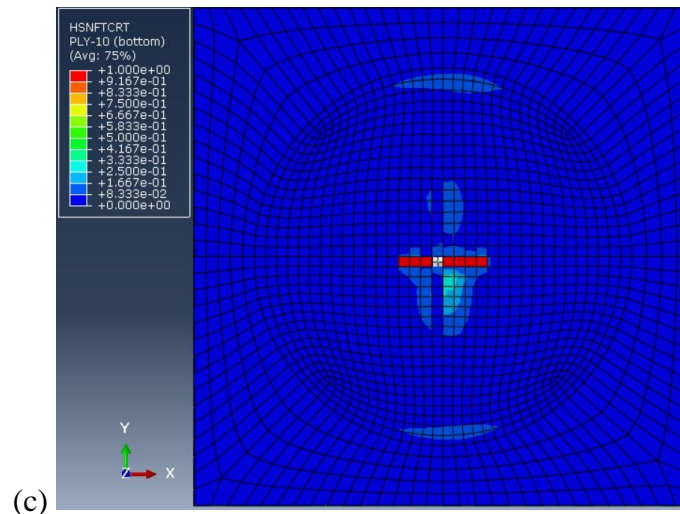
Moreover, the predicted tensile matrix damages on the top and bottom layer were demonstrated in Figure 4.7 (e) and Figure 4.7 (f), respectively. Here, the area of matrix

damage is much wider than the fiber damage. Also, the matrix damage initiates at an

earlier stage than the other damages, and such phenomena were mentioned in Chapter 1.

(e)

(f)
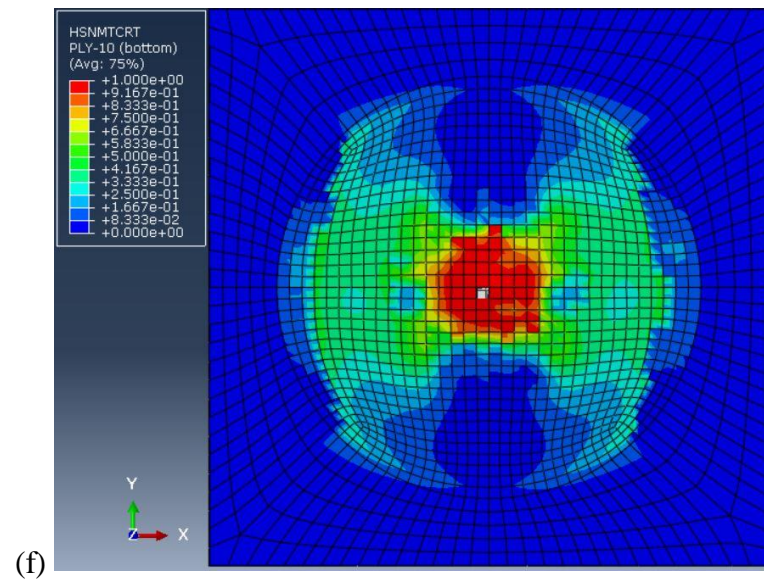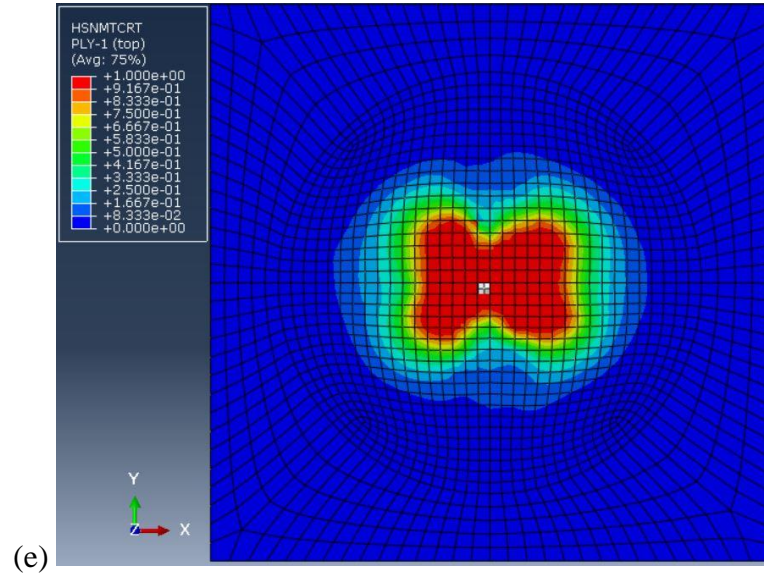
Figure 4.7 Tensile fiber damage a) initiation and b) completion at the top (impacted) layer. Tensile fiber damage c) initiation and d) completion at the bottom (unimpacted) layer. The tensile matrix damage completion at the e) top layer and the f) bottom layer.

5. Structural Optimization

In this Chapter, the focuses were on improving the damage tolerance and decreasing the weight of the existing composite plate used in the LVI testing and simulation. The optimization software used was MSC. NASTRAN with the coding based on patran command language (PCL), and MSC. PATRAN that created the input model. Thus, the first step is to set up the model in MSC. PATRAN with similar analysis parameters used in ABAQUS. Also, the analysis type was solution 400 (SOL 400), nonlinear transient response analysis.

Then, the possibility of using the framework OpenMDAO with SciPy optimizer to deal with sizing optimization was explored based on the model created from SOL 400. To solve such a nonlinear problem, the interface between SciPy and MSC. NASTRAN was built. Except for MDAO, prior researchers have studied accomplishing optimization under nonlinear dynamic loading. Lee and Park (2011) had used the approximation method which is the response surface method (RSM) to do shape optimization of the initial blank in the sheet metal forming process.

Also, a less computational optimization method, equivalent static loads (ESLs) was used to transform the nonlinear dynamic loads into ESLs, and the ESLs would be utilized as external loads in the linear response optimization. These two methods (ESL & RSM) seem feasible in this study, but according to the knowledge of the author, there was no similar study done on the LVI optimization of composite laminates.

Due to the lack of research resources, the traditional optimization codes solution 200 (SOL 200) was used to perform sizing and shape optimization in this research. However, the analysis of nonlinear dynamic response is not supported in SOL 200, see Figure 5.1.

Thus, a compromised model of linear modal transient analysis (SOL 112) was used, and the output results were close to the ones from SOL 400. Therefore, the size optimization results from SOL 200 and SciPy would be compared, and hence the difference between these two methods would be clearer. Moreover, the improvement of the damage resistance of the laminates would be measured based on the values of structural responses used in the constraints.

As for shape optimization, the OpenMDAO/SciPy does not have the capability. Thus, SOL 200 was applied in two methods, the direct input shape method and the geometric boundary shape method. Their results would be shown respectively.

Analysis	SOL Numbers	Multiple Subcases	Multiple Boundary Conditions
Statics	101	Y	Y
Normal Modes	103	Y	Y
Buckling	105	Y	Y
Direct Complex Eigenanalysis	107	N	N
Direct Frequency	108	Y	Y
Modal Complex Eigenanalysis	110	N	N
Modal Frequency	111	Y	Y
Modal Transient	112	N	N
Static Aeroelasticity	144	Y	Y
Flutter	145	Y	Y

Figure 5.1 Analysis disciplines supported in SOL 200 (MSC Nastran user's guide design sensitivity and optimization, 2017).

5.1. Original Finite Element Analyses

In this subsection, the FEA of nonlinear dynamic response using SOL 400 and the modal transient response using SOL 112 would be shown. Besides, the displacement and contact stress results from SOL 400 would be used to implement sizing optimization with OpenMDAO/SciPy optimizer, and the displacement result from SOL 112 would be

conducted the sizing optimization again and the redesign was compared with the one

from SciPy. Then, two shape optimization methods were introduced that can further

develop the damage resistance of the composite laminates at a lower cost.

5.1.1. Nonlinear Dynamic Response Analysis

The LVI model was replicated in MSC. PATRAN with the same composite material

properties, loading, and impact parameters. The analysis type used was SOL 400, it

allows for an easy transition from linear to nonlinear analysis inside one tool. The LVI

cases could be solved from the advanced element technology of SOL 400 that handles

large deformation while maintaining an accurate nonlinear strain-deformation

relationship. The nonlinear analyses are performed based on the incremental loads, where

each increment is solved iteratively to ensure equilibrium of the external and internal

loads.

As shown in Figure 5.2 only a quarter model was created because of symmetry, and it

helped to simplify the FEA for the optimization process while maintaining the same

output compared to the complete model. The central node as node 1, and there were 4

outer edges in total on the plate. Also, the boundary condition applied on the composite

plate was changed accordingly, the degrees-of-freedom (DOF) was based on the

translational and rotational direction.

In Table 5.1, number "1-3" denoted the components that were fixed in the

translational directional direction of "XYZ", while the number "4-6" denoted the

components that were fixed in the rotational direction of "XYZ". The Quad4 shell

element was used to model the plate. Also, the plate was separated into the regions "1-4",

and region 1 was the impact zone. Different mesh sizes were also used for the impact

zone and untouched zone. In the central impact zone, the mesh size was the same value used in ABAQUS. The shear deformation theory was chosen. The initial speed of the impactor was set to 2.0 m/s.

The mesh in the untouched zone decreased progressively to the end of edge 1 and edge 2, and it was proportional to the length of the edges. The impactor and the plate were defined as two deformable bodies for the contact analysis, and the general contact method helped to automatically detect the contact "master body" and the "slave body" that being contacted, and it was able to determine the contact region based on the contact elements. The total impact time was set as 10 ms, with the time increment of 0.2 ms based on the automatic stepping schemes. Moreover, the Hashin failure criteria were also included.

Several output response results were obtained since the optimization using the SciPy optimizer could track the displacement and the normal contact stress responses and select the peak values as the constraints, only these two responses were selected and shown in Figure 5.3 and Figure 5.4. There, the peak nodal displacement happened on node 1 at 4.4 ms, which was 6 mm. The peak normal stress happened on node 18 (located in the red grid point) at the same time, which was 358 MPa.

Table 5.1

Boundary constraints of the model

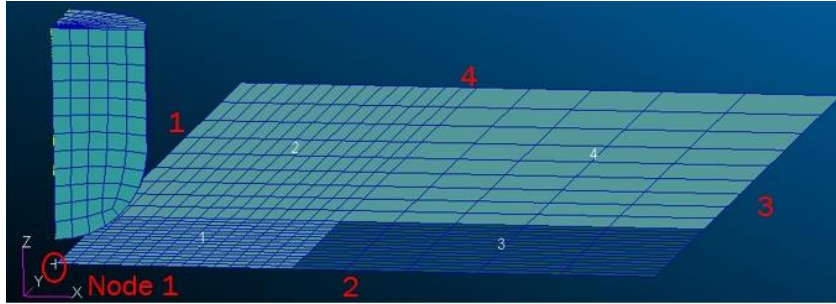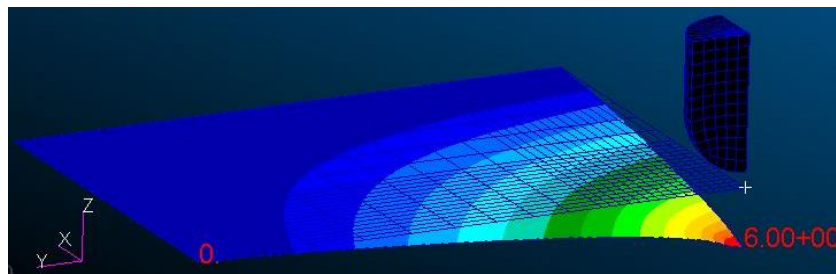|	Translational Direction	Rotational Direction
Node 1	1 2	4 5 6
Edge 1	2 3	5
Edge 2	1 3	4
Edge 3	1 2 3	4 5 6
Edge 4	1 2 3	4 5 6

Figure 5.2 LVI model of SOL 400.

Figure 5.3 Maximum displacement on node 1.
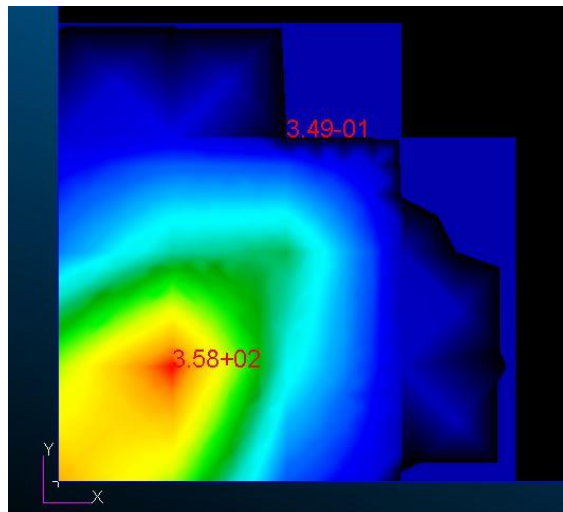
Figure 5.4 Normal contact stress (node 18 shown in red).

5.1.2. Linear Transient Analysis

As mentioned earlier, the SOL 200 could not perform the optimization with nonlinear

dynamic loading. Thus, an alternative method was used with the linear transient analysis

(SOL 112) that could simulation the LVI testing. In the model of SOL 112, the impactor

and the properties of it was deleted. Besides, the model was combined with the Tsai-Wu

failure criteria. Instead of using the initial speed of the impactor, the time-dependent

contact forces from SOL 400 would be the input nodal loading in the SOL 112 case.

From the contact state development animation from SOL 400 and is also shown in *Figure*

5.4, the real-time contact is focusing on the central element 1, which lead to the stress

concentration on node 18.

In element 1, the four nodes were nodes 1, 2, 17, and 18. Thus, the nodal force history

was extracted from SOL 400 and selected as the input for SOL 112, and the plots are

illustrated in *Figure 5.5*. In the model of SOL 112, these nodal forces would be applied

to the corresponding nodes in the impacted element. In the following subsections, the

output displacement result from SOL 112 was utilized to define the boundaries of the

constraints.

Meanwhile, the peak displacement value of node 1 is provided in *Figure 5.6*. The

peak value was 6.91 mm at 5 ms. From the plot, it could conclude that the displacement

results were similar between SOL 112 and SOL 400, which lead to the good agreement of

these two methods. However, the gaps between these two curves could be due to the

failure criteria, and the higher peak displacement from SOL 112 may be caused by the

localized nodal forces.
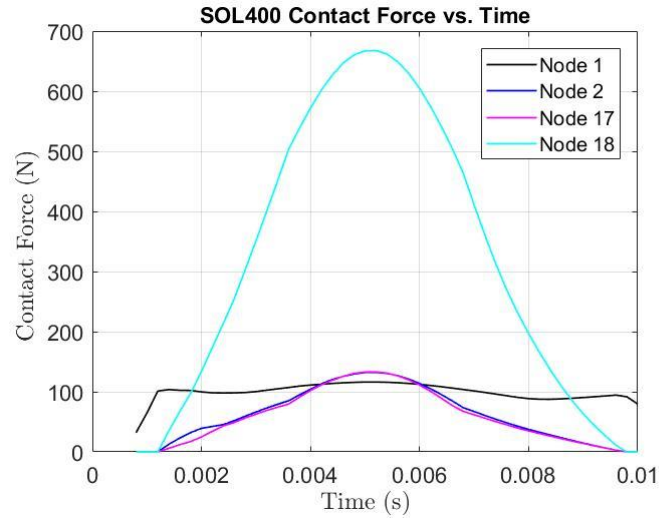
Figure 5.5 SOL 400 nodal contact forces history.
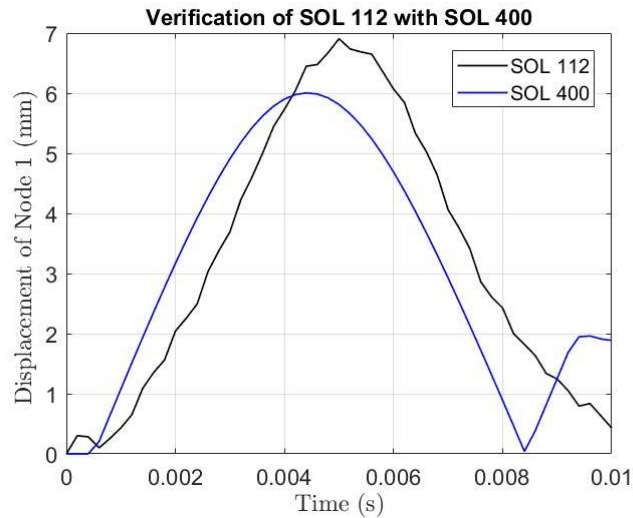
Figure 5.6 Displacement history of SOL 112 and SOL 400.

5.2. Size Optimization

In this section, two sizing optimization cases would be presented, one based on the

SOL 200, the other depends on the SciPy optimizer. Both of the cases have 20 design

variables, which are 10 variables for the 10-ply thickness (X_1, X_2, …, X_{10}), and 10

variables for the orientation of each ply (X_{11}, X_{12}, …, X_{20}). Also, the objective of both

cases will be minimizing the mass (m) of the composite laminate plate, and the expression could be written in the forms of length (L), width (W), total plate thickness (T), and the value of density (ρ). The constraints could be regarding the nodal displacement (δ) or nodal contact stress (σ), depending on the optimization cases. Also, the values of the variables would be limited in a feasible range. The formulation for the sizing optimization process is shown below,

$$\text{Min } m = L \cdot W \cdot T \cdot \rho \tag{40}$$

Where,

$$T = \sum_{0}^{10} X_i, \quad i = 1, ..., 10 \tag{41}$$

Subject to,

$$0 < X_i \leq 0.4, \quad i = 1, ..., 10 \tag{42}$$

$$270 \leq X_i \leq 450, \quad i = 11, ..., 20 \tag{43}$$

$$\delta \leq \delta_{Allowable} \tag{44}$$

Or/And

$$\sigma \leq \sigma_{Allowable} \tag{45}$$

In Equation 40, the initial value of the objective could be calculated using the density properties in Table 4.1, the known length and width of the plate, and the thickness of the layers. Here, the initial plate mass is obtained as 11.62 g.

5.2.1. Size Optimization with SOL 200

Here, the model from SOL 112 was used, and it was translated into the PCL based coding. To form the optimization task, the design model was defined as supplementary sources, and the objective, design variables, constraints were inserted in the coding. In Table 5.2, the bulk data entries briefly demonstrated how these items were defined. Therefore, the 20 design variables were defined by the DVPREL1 entries, and the upper bound values and lower bound values were input in the DESVAR entries. Considering the efficiency, only half of the variables were selected their boundary values, and the rest 10 were linked with the DLINK entry. Also, the redesigned ply angles were limited to the discrete values from $0°$ $(270°)$ to $90°$ $(450°)$ with an increment of $5°$. Besides, the layup should end up with a symmetric configuration instead of the initial cross-ply. Also, all the ply thickness after optimization should be equal.

Thus, the relations were set up using the DDVAL entries. For this case, the constraint value, $\delta_{Allowable}$, was selected as the displacement of node 1, and the value should be within 6mm (around 87% of the original peak value from the FEA). The value of the constraints were defined with DRESP1 and DCONSTR entries. Moreover, the maximum iteration number of the optimization task was set as 30 cycles, the minimum design variable move limit was 0.1 (default value is 0.05), and those analyzing properties were defined with the DOPTPRM entry.

Next, the objective and constraints were all mentioned in the case-control section which is above the bulk data section, and these two were identified. Also, the output requirements as the displacement history, objective history, and constraint history during each design cycle were included in the case-control section. In the same section, the

quantity of the node 1 displacement was selected as output. After the optimization task was terminated, the history file would include all the changed property values.

Table 5.2

Bulk data entry descriptions

Entry name	Descriptions
DVPREL1	Defines the relation of the model property with the variables
DESVAR	Defines the design variables
DLINK	Relates a variable with more others
DDVAL	Defines discrete design variables values
DRESP1	Defines the structural responses as an objective or as constraints
DCONSTR	Define design constraints
DCONADD	Defines the constraints as a union of DCONSTR entries
DOPTPRM	Override default values of the parameters

The sizing optimization terminated due to hard convergence to a best compromise infeasible design after 26 design cycles. Below, Figure 5.7, Figure 5.8, and Figure 5.9 show the value changing history of the objective, constraints, ply angle, and ply thickness, respectively. In Figure 5.7, it is seen that the objective decreased to 4.13 g after the first design cycle and increased rapidly till 12.45 g at the end, which resulted in a 7.14% increase in the initial mass value. Therefore, it was not a feasible design result. However, the maximum value of the maximum normalized constraint started from 0.205 and dropped to 0.853E-3 at the end. The normalized constraint was mentioned in Chapter 2, when the value reaches +1, it represents a 100% violation irrespective of the magnitude of the response or whether it is an upper or lower bound.

From the plot, the positive constrain value indicates the infeasible design. Whereas, it decreased by the end, which shows the design was a compromise design and meets the displacement constraint limit. The reason for the unsuccessful redesign could be explained by the thin laminates, which is a lack of bending stiffness, and the through-thickness strength is poor. Thus, if a thicker laminate were used, the redesign should give a better result. However, the shape optimization in the following sections would avoid such failure and bring many improvements.

In Figure 5.8, since the redesign was to form a symmetric laminate, the plies with an initial value of $0°$ would change in consistent, the curves would overlap with each other during the cycles, and shows in one "orange" curve. The same thing happened for the $90°$ plies and the value changings were shown in the "yellow" curve.
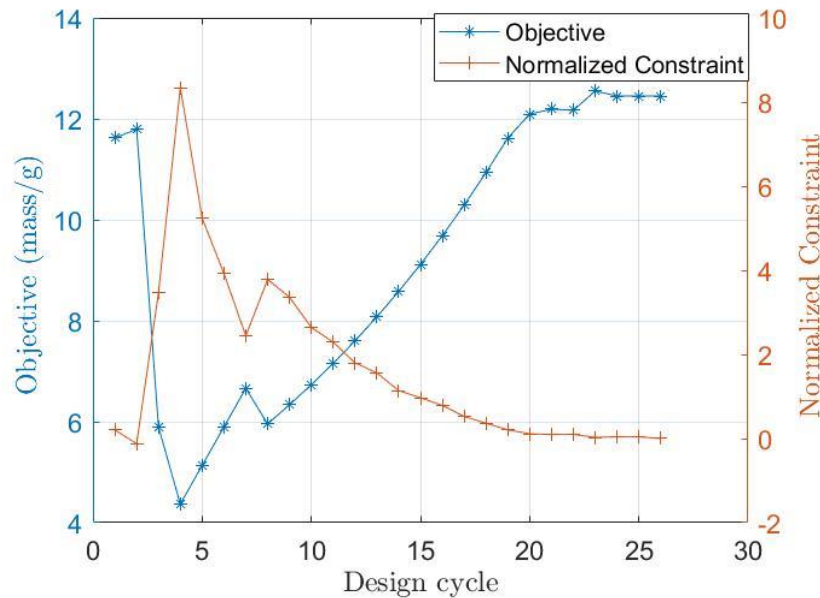
Figure 5.7 Objective and constraint history of SOL 200.
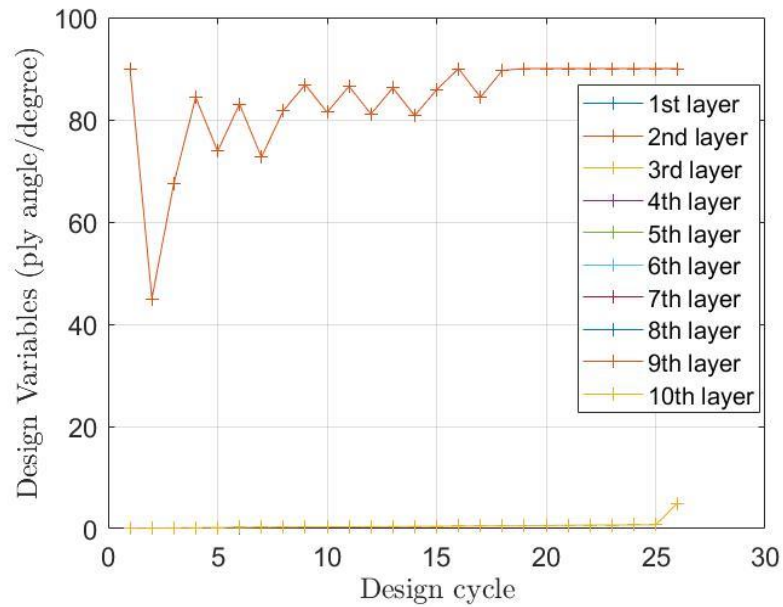
Figure 5.8 Ply angle history of SOL 200.

In Figure 5.9, the thickness changed in consistency during optimization, and the value increased a little bit, which leads to the increase of the objective. In Figure 5.10, it shows clearly that the peak displacement of node 1 decreased from 6.91 mm to 5.98 mm when using SOL 112, which satisfied the constraint limit and accomplished a 13.46% decrease. Moreover, the node 1 peak displacement is within the constraint range after using the redesigned size parameters with SOL 400.

The response curves of SOL 112 and SOL 400 are similar, while the impact duration is shortened with SOL 112 and the corresponding peak value obtains at 4.2 ms. The differences between the two models could be due to the inaccurate loading applied, where the nodal forces would not simulation the real LVI, and the SOL 112 is not capable of computing such a complex nonlinear process. In Table 5.3, a brief conclusion of the redesigned parameters is demonstrated.

Figure 5.9 Ply thickness history of SOL 200.

Figure 5.10   Node 1 displacement comparison before and after size optimization.

Table 5.3

Results of sizing optimization using SOL 200

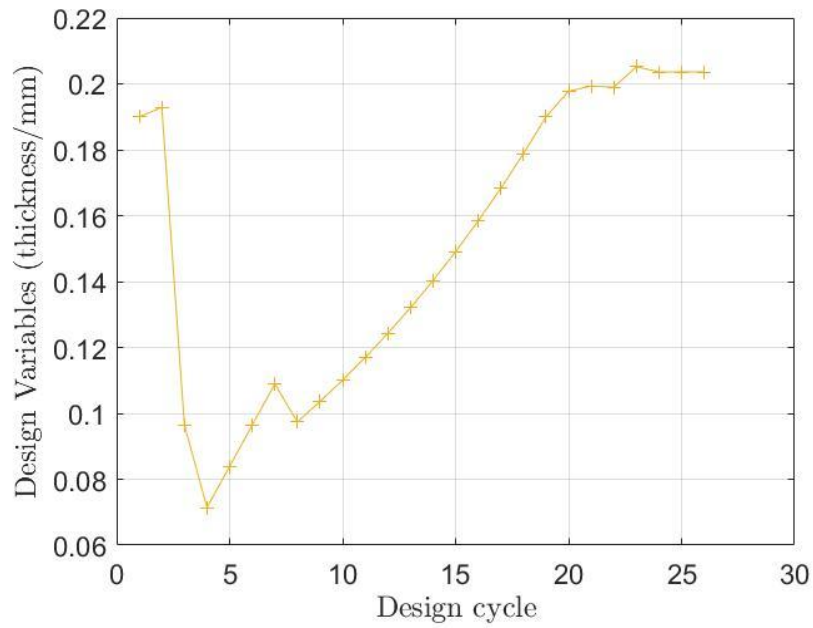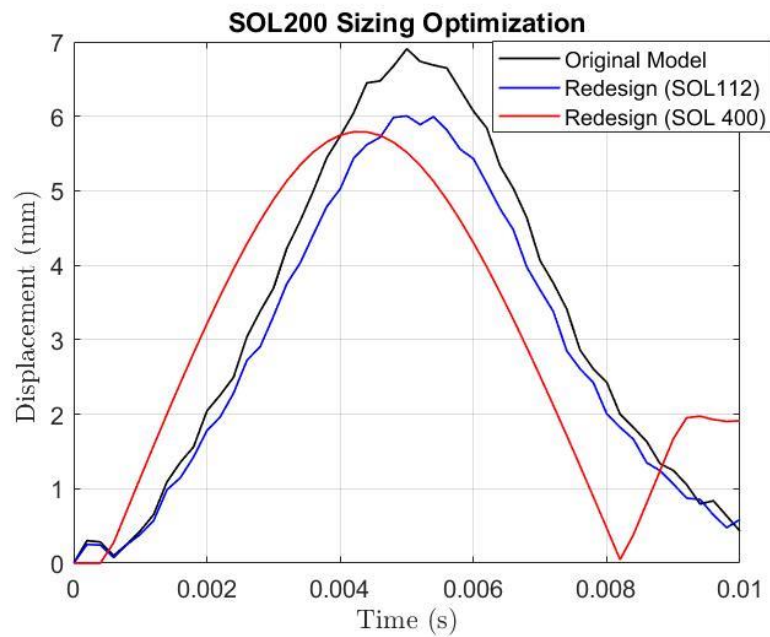| Property type	Initial value of the properties	Final value of the properties after 26 cycles
X_i, i=1, … , 10	0.19 mm	0.236 mm
$X_{11}, X_{13,} X_{15}$	$0°(270°)$	$5°(275°)$
$X_{16}, X_{18,} X_{20}$	$0°(270°)$	$5°(275°)$
$X_{12,} X_{14}$	$90°(360°)$	$90°(360°)$
$X_{17,} X_{19}$	$90°(360°)$	$90°(360°)$
Objective m	11.62 g	12.45 g
Peak displacement δ	6.9 mm	5.98 mm (SOL 112), 5.79 mm (SOL 400)
CPU time: 97 s		
Total number of NASTRAN run of FEA: 27		

5.2.2. Size Optimization with OpenMDAO/SciPy

The OpenMDAO originated in 2008 by Moore et al. (2008) at NASA. Gray et al. (Gray et al., 2019) had developed the new version OpenMDAO V2 based on the first version of Open MDAO V1, which was based on the framework of the open-source multidisciplinary design optimization (MDO), it could deal with coupled systems through Newton-type algorithms and solve structural optimization task by introducing new hierarchical strategies.

Typically, MDO enables interdisciplinary interactions when implementing the coupled analysis. Also, the optimization could deal with all the design variables simultaneously. The success of the MDO largely relies on the efficiency of analysis and optimization. The coupled analysis uses the Newton-type methods is more efficient, and the gradient-based optimization methods work better than the gradient-free methods. Besides, compared to the previous version OpenMDAO V1, one significant improvement of the new version was that it could calculate the total derivatives of the model outputs with the corresponding inputs.

Generally, OpenMDAO can compute total derivatives with three inserted methods in one framework, finite difference, complex-step, semi-analytic, and analytic methods. Among these methods, the analytic methods are the most welcomed because of the accuracy and efficiency, and they could be classified into the direct method and the adjoint method. To simplify the theory of different methods computing the derivatives, the unified derivatives equation shows all the methods that derived from one equation, and it allows the possibility of larger and more complex problems to be solved. However, such a combination of derivatives computation was restrained by the serial computing capabilities.

Thus, Hwang and Martins (2018) had come up with the modular analysis and unified derivatives (MAUD) architecture, which could formulate the variables in a nonlinear problem to a single nonlinear equation (or a vector of all the unknowns, u). The main advantage of transforming the model to a single nonlinear expression is that the unified derivatives equation could be used, and the form of the equation is shown in Equation 46.

$$\left[\frac{\partial R}{\partial u}\right]\left[\frac{du}{dr}\right] = \left[\frac{\partial R}{\partial u}\right]^T\left[\frac{du}{dr}\right]^T \tag{46}$$

Here, the MDO model is expressed as $R(u) = 0$, where R is the residual functions that make the modified system the same as the original one. The du/dr includes a set of total derivatives that we want at the end. Such transformation results in a larger implicit system that has all the intermediate variables from the whole model. Therefore, the system is more difficult to converge. Thus, the OpenMDAO V2 offers a hierarchical Newton method based nonlinear strategy. It solves each subsystem first and saves the overall computational cost.

In this research, the OpenMDAO V2 was worked with the SciPy optimizer, which was solved in sizing optimization under LVI. The solver of the SciPy optimizer leveraged the sequential least squares programming, and the maximum number of iterations was 20. Also, the precision goal of the objective function in the stopping criterion was 1.0 E-2 (default=1.0 E-3), and the step size for finite difference was 5.0 E-2 (default=1.0 E-3). In Figure 5.11, it shows how the local MSC. NASTRAN communicate with the OpenMDAO and Scipy optimizer.

Figure 5.11 File interaction between OpenMDAO/SciPy and MSC. NASTRAN.

First, a command was added to the original SOL 400 model created with MSC. PATRAN to output the .H5 file, in which all the responses from the LVI analysis were captured. These responses could be selected as objectives or constraints later. After analyzing the modified model, the .H5 file would be used for OpenMDAO. When the model file was uploaded to OpenMDAO, the design variables were defined as both the ply thickness and ply orientation of the 10 plies. The .H5 was then uploaded. Although the OpenMDAO is developed by Python programming language, it could link the PCL language-based .H5 file and extract all the responses.

Then, the objective was set to minimize the mass of the plate, which was 1.694 kg (included one-quarter mass of the hemispheric impactor and the plate). The constraints were selected as the displacement and normal contact stress of node 1 and node 18 for the two subcases, respectively. After a series of attempts using different constraint limits and

adjusting the convergence parameters, the upper limit of the constraints could not be further decreased below 93% of the original peak value from the FEA, or the optimization may end up to failure.

Thus, for the displacement case (subcase 1), the final value of the nodal displacement during all the time steps should not exceed 5.6 mm (93.2% of the original peak displacement value of node 1). For the contact stress case (subcase 2), the final value of the normal contact stress of the whole impact process should not greater than 333.94 MPa (93.2% of the original peak stress value of node 18).

After 4 design cycles, the sizing optimization of subcase 1 was terminated. The task took 7920 CPU seconds to finish. The parameter changing histories are shown below in Figure 5.12, Figure 5.13, and Figure 5.14.

Figure 5.12 shows a similar plotting trend with the ones using SOL 200 (Figure 5.7). Since the objective increased by 0.13% from 1682.13 g and the constraint decreased from 0.111 to 4.23 E-4, it indicates a best compromised infeasible design. In Figure 5.13 and Figure 5.14, the values changing history of the ply angle and ply thickness of each layer are illustrated. In Figure 5.15, the peak normal displacement starts from 6.01 mm (4.4 ms) and ends up to 5.60 mm (3.4 ms), which satisfies the constraint limit. For the optimized model, the variation of the ply angles and the increased thickness makes the maximum displacement come earlier under LVI, and shorten the impact duration time.
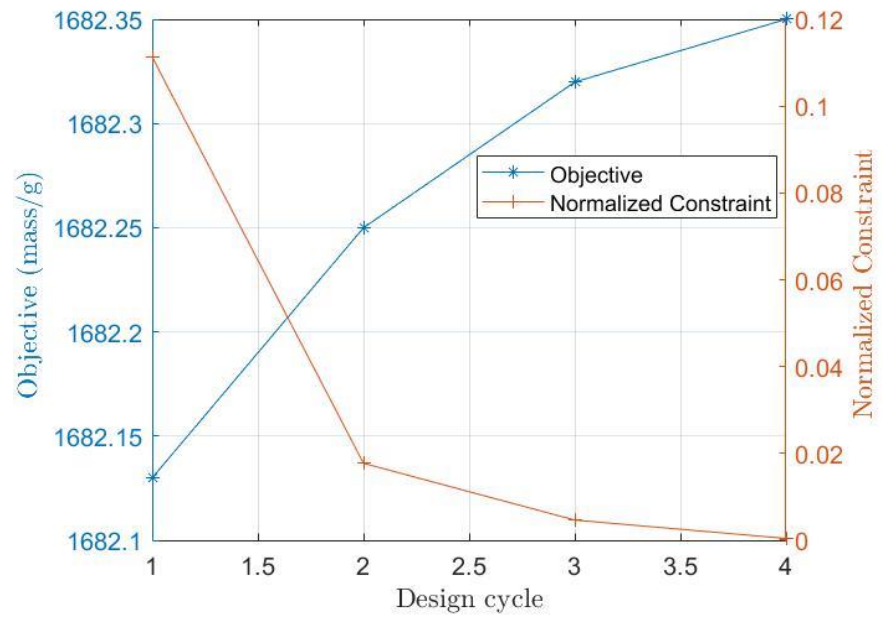
Figure 5.12 Objective and constraint history of OpenMDAO/SciPy (displacement).
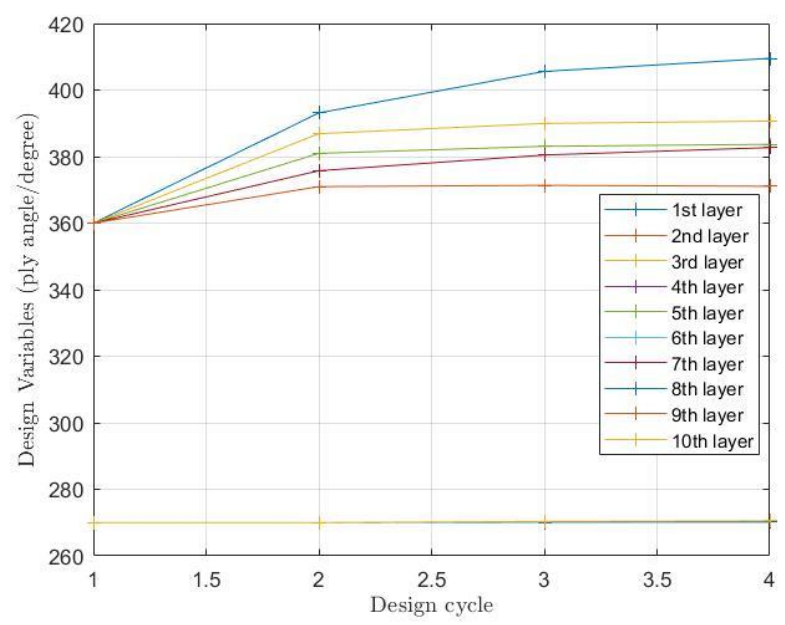
Figure 5.13 Ply angle history of OpenMDAO/SciPy (displacement).
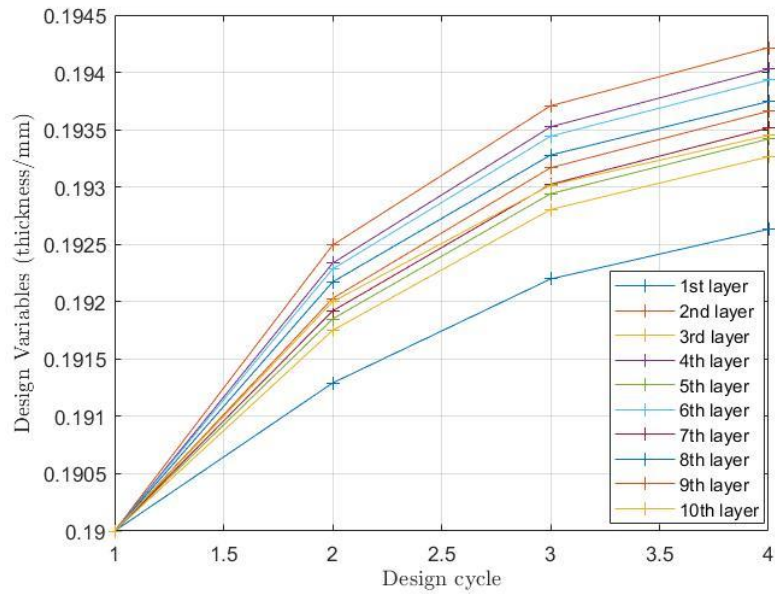
Figure 5.14 Ply thickness history of OpenMDAO/SciPy (displacement).
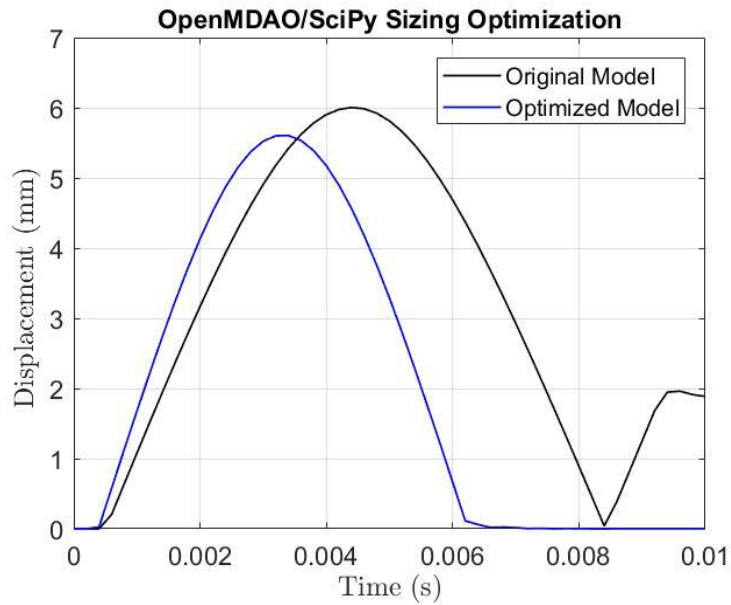
Figure 5.15 Node 1 displacement comparison before and after size optimization.

As for subcase 2, the optimization task ended in 3 design cycles and achieved hard

convergence. The task took 7080 s CPU time till finishing. In Figure 5.16 and Figure

5.17, it is seen that the mass barely changes because the ply thicknesses only have little changes. However, the rearranging of the ply angles is the main reason for resulting in the decrease of the peak normal contact stress of node 18 in Figure 5.19. There, the peak normal stress of node 18 decreases from 358.31 MPa to 319.28 MPa. Also, it shows the values of the ply angles with the initial $0^{\circ}(270^{\circ})$ are changing more drastic than the $90^{\circ}(360^{\circ})$ ones. This case shows that even the mass (thickness) of the composite laminates plate remains unchanged, the redesign of the ply angles could be feasible to realize the goal of size optimization and satisfy the constraint requirements.
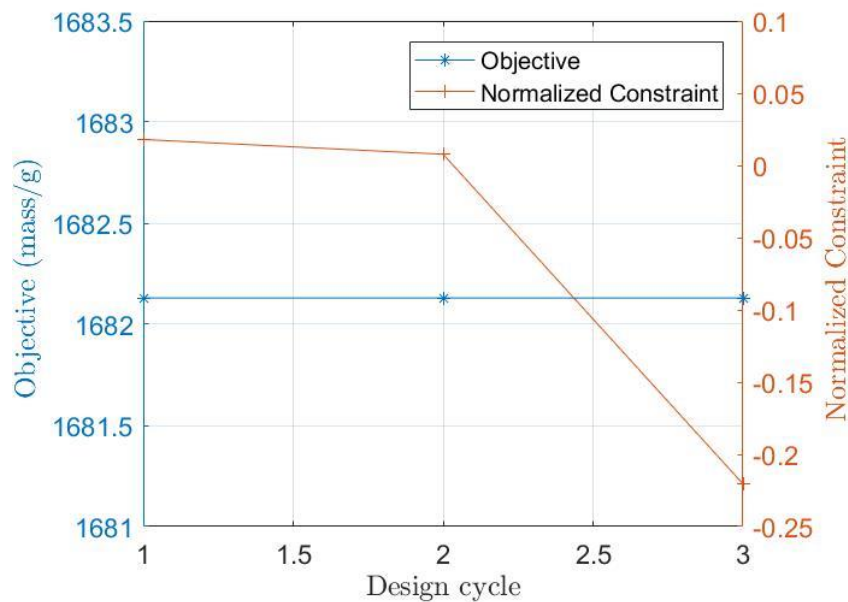
Figure 5.16 Objective and constraint history of OpenMDAO/SciPy (stress).
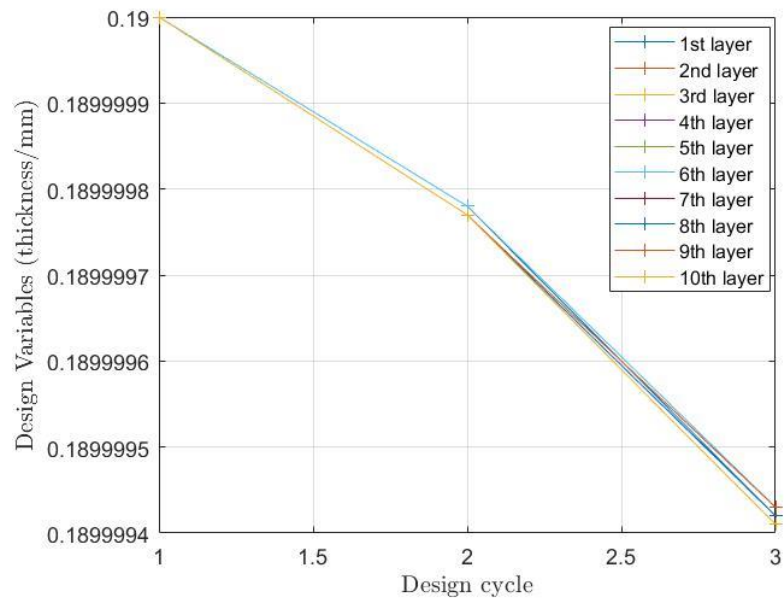
Figure 5.17 Ply thickness history of OpenMDAO/SciPy (stress).
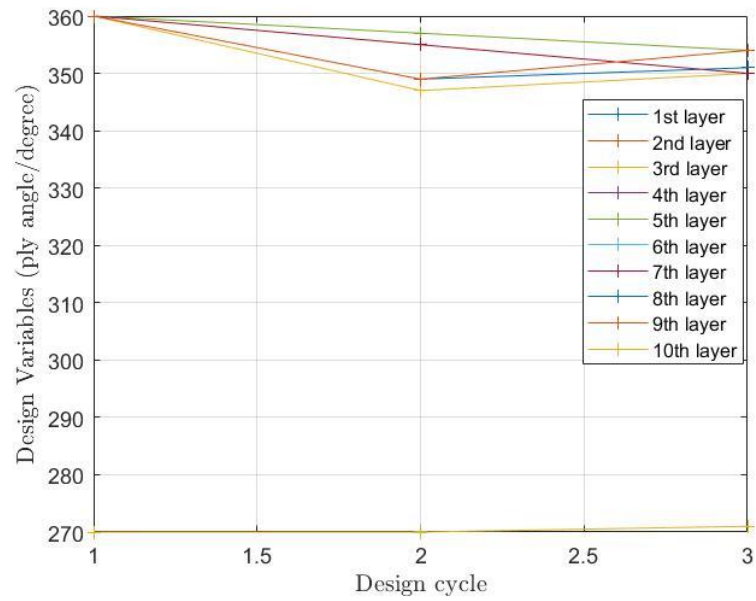
Figure 5.18 Ply angle history of OpenMDAO/SciPy (stress).
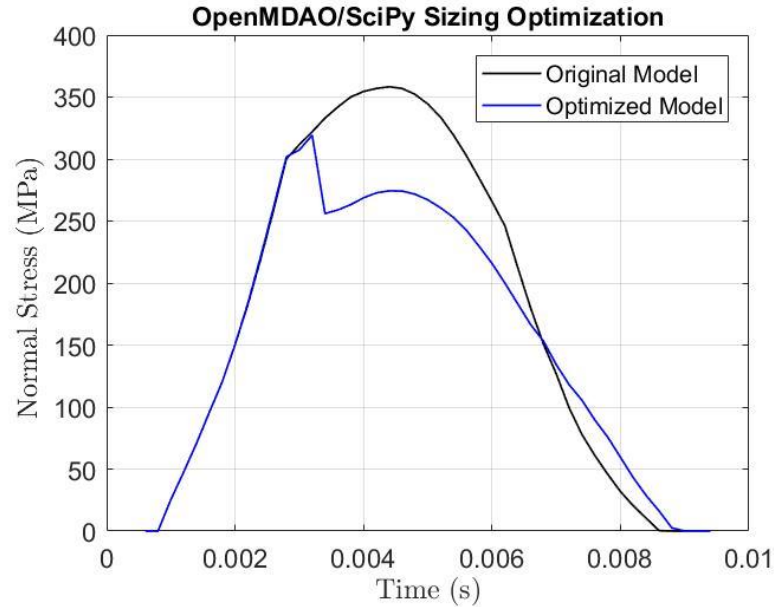
Figure 5.19 Node 18 normal stress comparison before and after size optimization.

Comparing the optimization methods of using SOL 200 and OpenMDAO/SciPy, SOL 200 took far less computational time, which was only 1.2% - 1.3% of using the OpenMDAO/SciPy. However, regarding the number of NASTRAN run of sensitivity analysis, the SOL 200 performs analysis needs one NASTRAN run to solve the analysis of all the variables in each design cycle.

If choosing OpenMDAO/SciPy, the sensitivity analysis performs on each design variable, and the NASTRAN runs 20 times for the 20 variables in one design cycle. Thus, the latter requires much more time for sensitivity analyses, and all add up to the computational time. Except for the computational efficiency, the accuracy is more vital. The OpenMDAO allows us to simulate the nonlinear dynamic loading from SOL 400, it gives more realistic results from the LVI cases. Also, when one design variable is updated after the redesign, the sensitivity analysis would be performed, and the

constraints in the whole-time range are considered, which further consolidates the accuracy of the design task.

5.3. Shape Optimization

The shape optimization is much more computationally expensive and complex than sizing optimization. Shape sensitivity and optimization in MSC. NASTRAN needs the design variables, shape basis vectors, and the relation between the vectors and variables. Here, the shape of the structure is defined as the variable by redesigning the grid nodes on the boundary and update the mesh to a linear field. The shape basis vector defined from the auxiliary model or manual input would affect the grid points. Then, it leads to the change of variables in the design cycles and gets the shape change.

Based on the sequential quadratic programming (SQP) algorithm, in each cycle, a line search (together with the variables) is implemented, and the value of the objective function would be calculated along the search until an improved design appears. Such a gradient-based search requires the first derivative of the objective concerning the variables (Johnson & Wächter, 2015). The gradients could be obtained by the discrete model-based direct method or the continuous based adjoint method.

In SOL 200, four shape optimization methods are supported, the manual grid variation method, the direct input of shapes method, the geometric boundary shapes method, and the analytical boundary shapes method. Compared to the manual grid variation method, the geometric boundary shapes method is like an improved version, and it is more efficient that produces the optimization code automatically. For the analytical boundary shapes method, it is more frequently used on complicated structures with complex requirements on the shape change. In this case, the composite plate is not

that sophisticated, and the direct input of shapes method is more applicable while maintaining good accuracy. Compared to Equations 40-44, the formulation of the shape optimization becomes:

$$\text{Min } m = L \cdot W \cdot T \cdot \rho \tag{47}$$

Subject to,

$$0 < L \leq 76.2 \tag{48}$$

$$0 < W \leq 50.8 \tag{49}$$

$$\delta \leq \delta_{\text{Allowable}} \tag{50}$$

Here, the length (L) and width (W) of the plate were chosen as the design variables, while the total thickness (T) and density (ρ) were constant. Since the shape optimization could further improve the design than sizing optimization, the value of $\delta_{\text{Allowable}}$ was further decreased to 5.5 mm (79.71% of the original peak displacement form SOL 112).

5.3.1. Shape Basis Vector

The optimizer would determine the proper shape basis vectors, and a simple introduction of the function of these vectors is shown below. Assume an angle bracket redesign task, the outer edge should be straight while changing the length of the bracket in both the X-axis and Y-axis. The model is seen in Figure 5.20, and the grid locations could be expressed in Equation 51.
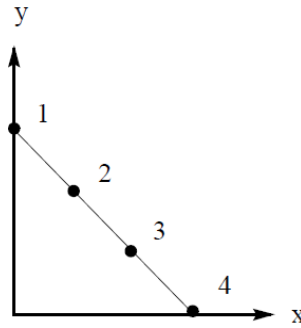
Figure 5.20 Initial angle bracket.

$$\begin{Bmatrix} G_{2x} \\ G_{2y} \\ G_{3x} \\ G_{3y} \end{Bmatrix} = \begin{bmatrix} 0 & 1/3 \\ 2/3 & 0 \\ 0 & 2/3 \\ 1/3 & 0 \end{bmatrix} \begin{Bmatrix} G_{1y} \\ G_{4x} \end{Bmatrix} \tag{51}$$

When considering the grid change, the vector change on the coordinate could be reflected in the variable. In Equation 51, the columns in the matrix on the right side are the shape basis vectors. Then, the grid variation is considered. Thus, the vector changes could be illustrated in Figure 5.21, where includes both shape variation in the vertical and horizontal directions. Likewise, the relation between the variables and basis vectors in Equation 51 is then shown in Equation 52. The new grid location is also shown in Equation 54.
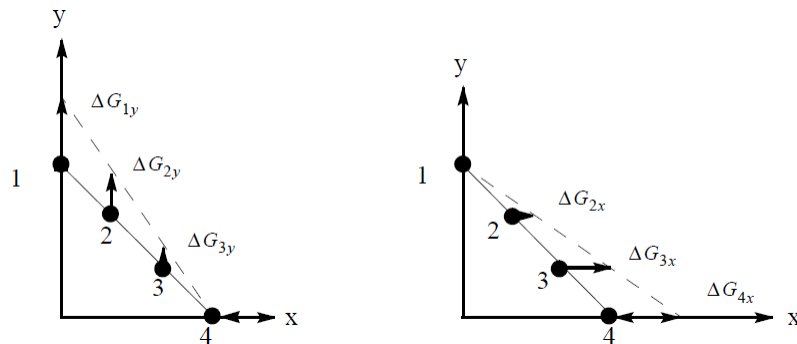
Figure 5.21 Shape vectors of the brackets.

$$\begin{Bmatrix} \Delta G_{1y} \\ \Delta G_{2x} \\ \Delta G_{2y} \\ \Delta G_{3x} \\ \Delta G_{3y} \\ \Delta G_{4x} \end{Bmatrix} = \begin{bmatrix} 1 & 0 \\ 0 & 1/3 \\ 2/3 & 0 \\ 0 & 2/3 \\ 1/3 & 0 \\ 0 & 1 \end{bmatrix} \begin{Bmatrix} \Delta x_1 \\ \Delta x_2 \end{Bmatrix} \tag{52}$$

$$\{\Delta G\}_{m \times 1} = [T]_{m \times n} \{\Delta x\}_{n \times 1} \tag{53}$$

$$\{G\}_{new} = \{G\}_0 + [T]\{x_{new} - x_0\} \tag{54}$$

5.3.2. Auxiliary Model

The auxiliary model was used in the direct input method to create shape basis vectors. An auxiliary model often has the same geometry, element connectivity, and material type as the original model. However, the boundary conditions could vary, the loading applied to this model helps to get the displacement vectors, and these vectors could be easily utilized as shape basis vectors for shape optimization. Also, several auxiliary models could be modeled simultaneously to get more possible vectors. In the original model from SOL 112, we want to decrease the weight of the plate by decreasing both the length and width of it. Therefore, the loading used in the auxiliary model should be able to "shrink" its dimensions.

Thus, two auxiliary models were used, one to create the basis vectors in the length direction (Y-axis), and the other creates basis vectors in the width direction (X-axis). The first model in Figure 5.22 (a) applied distributed enforced displacement of -10mm in the Z-direction to shorten the length, and created basis vectors in that direction. The bottom edge was fixed for all the six DOF, while the rest three edges allowed to move in the Z

direction. The second model in Figure 5.22 (b) used the same amount of enforced displacement in the X-direction.

The left edge of the model was fixed, while the rest three could move in the translational direction of the X-axis. Here, the deep blue gridding is the model without the loads, and the colorful triangular region shows the deformed plate after the static loading analysis. Therefore, two sets of basis vectors were obtained.
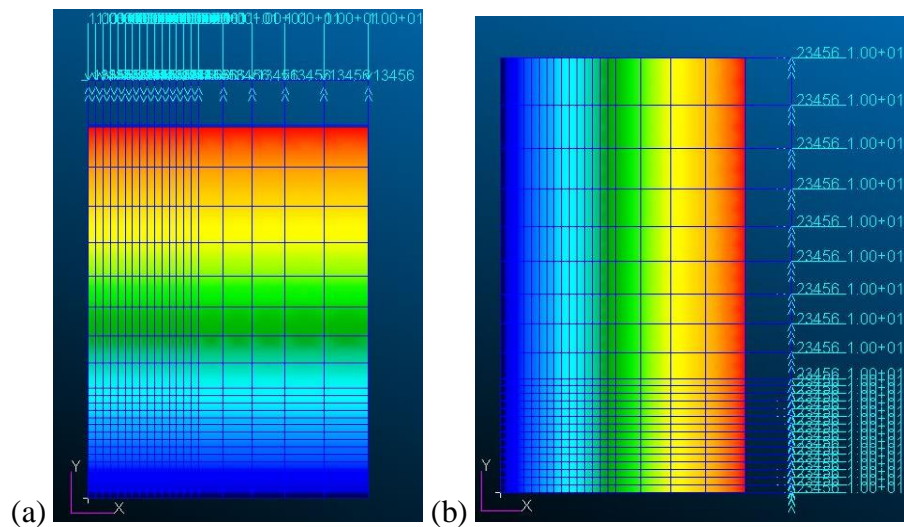
Figure 5.22 Auxiliary models: a) length direction, b) width direction.

5.3.3. Direct Input of Shape Method

This shape optimization method greatly simplifies the process of creating shape basis vectors. These vectors would be created externally from the auxiliary models that produce deformation on the grid points. Thus, the analysis would use this deformation as candidate shape changes. Like sizing optimization, the objective, constraints, and design variables were defined with the entries in Table 5.2. In addition, by using the DVSHAP

entry in the bulk data section, the basis vectors would be associated with the design variables and result in shape changes.

However, there are limitations to this shape optimization method, the basis vectors are not updated for each design cycle, and improper vectors could lead to mesh distortion. In Figure 5.23 and Figure 5.24, the value changing history of the objective, constraint, and design variables are shown respectively. After 7 design cycles, the feasible design results were obtained due to hard convergence. In Figure 5.23, the value of the objective decreased from 11.62 g to 8.50 g, which showed a 26.85% weight drop.

Also, the maximum constraint started in the infeasible domain and went into the feasible domain, and the final value was -0.05. In Figure 5.25, the peak displacement of node 1 dropped from 6.9 mm to 5.28 mm at 5 ms if using the SOL 112 model, and the value was within the range of the constraint limits. The optimized model of SOL 400 also satisfies the upper limit requirement and gives the peak displacement value of 5.45 mm at 4.2 ms. Thus, this shape optimization was completed successfully. Besides, Figure 5.26 shows the geometric changing of the plate before and after the shape optimization, where both the length and width are decreased. In Table 5.4, the brief conclusion of the redesigned parameters is demonstrated.

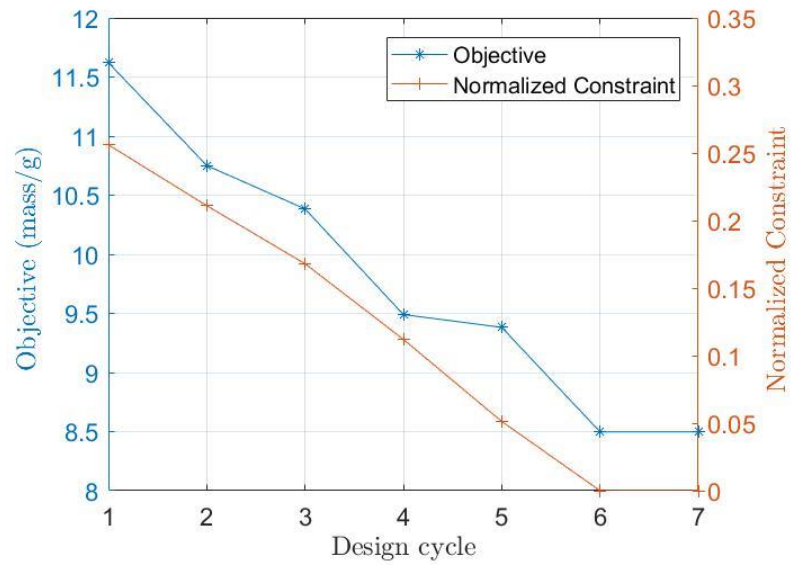*Figure 5.23* Objective and constraint history of direct input shape method.
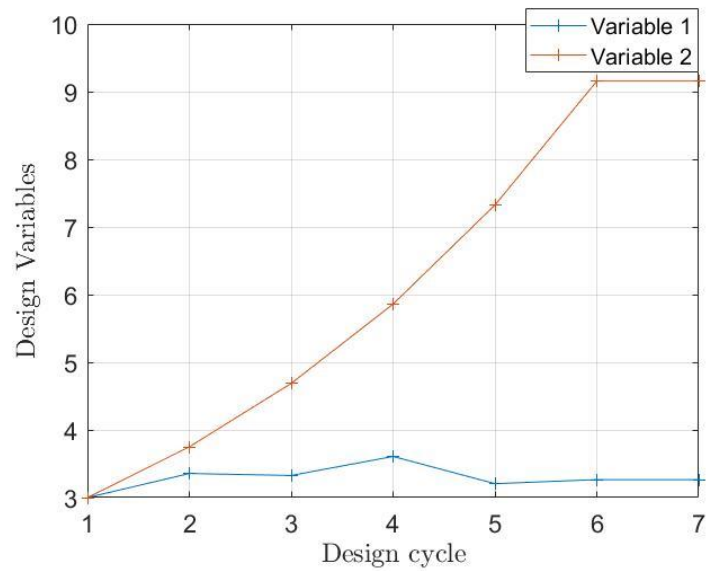
Figure 5.24 Design variables history of direct input shape method.

Figure 5.25 Node 1 displacement comparison before and after shape optimization.
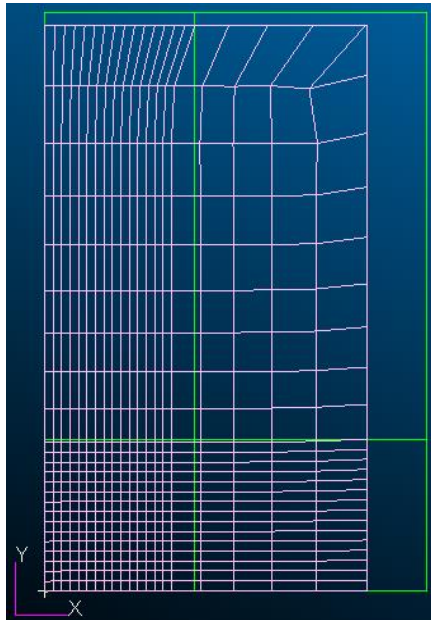
Figure 5.26 Composite plate before (green grids) and after (pink grids) direct input of shapes optimization.

Table 5.4

Results of direct input shape optimization using SOL 200

Property type	Initial value of the properties	Final value of the properties after 7 cycles
L	76.2 mm	73.54 mm
W	50.8 mm	38.49 mm
Objective m	11.62 g	8.50 g
Peak displacement δ	6.91 mm	5.28 mm (SOL 112), 5.45 mm (SOL 400)
CPU time: 76 s		
Total number of NASTRAN run of FEA: 8		

5.3.4. Geometric Boundary Shape Method

In this method, there's no need to create the auxiliary models to produce the basis vectors, and it applies a simpler way to get these vectors. It requires the users to define the expected shape variations only on the boundaries of the structure, this process is achieved with the BNDGRID entries by setting a list of grid point numbers on the boundaries. Besides, the DVGRID entries help to furnish the shape variation on the boundary. It would define the enforced displacement on the grid points of the boundaries, which creates the basis vectors, and the vectors will be associated with the design variables.

Therefore, the basis vectors for the whole structure are automatically produced by interpolating the boundary shape changes to the interior of the structure. In this case, we want both the length and width of the plate to decrease, so there will be two design variables regarding X-Y direction. For this method, the enforced displacements of -10 mm were applied on the boundary grid points in the X direction of edge 4 and Y direction of edge 3, and the location could refer to Figure 5.2. It was achieved with the DVGRID entry, and the resulted basis vectors were connected with the two variables, respectively.

Also, it is defined with BNDGRID entry that edge 1 and edge 3 were free to move in the T2 direction (translation direction of Y-axis), and edge 2 and edge 4 could move in the T1 direction (translational direction of X-axis).

 After running the shape optimization, it took 4 design cycles to hard convergence. In Figure 5.27 and Figure 5.28, the value changing history of the objective, constraint, and design variables are shown respectively. In Figure 5.27, the weight dropped by 17.13%, which is from 11.62 g to 9.63 g. Also, the value of the maximum normalized constraint is -0.032 at last, which proves the successful accomplishment of a feasible design task. In Figure 5.29, the peak displacement of node 1 is reduced by 25.94% of the original value and become 5.11 mm after optimization when performing SOL 112. The optimized model using SOL 400 has a slight surpass of 1.1% compared to the constraint upper bound value. Figure 5.30 shows the results after shape changes. Likewise, the conclusion of the parameter variation is provided in Table 5.5.
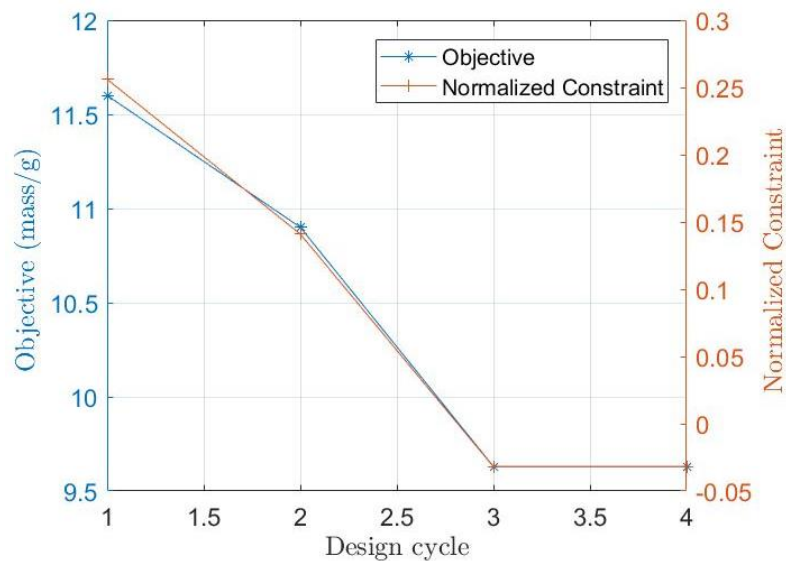
*Figure 5.27* Objective and constraint history of geometric boundary shape method.
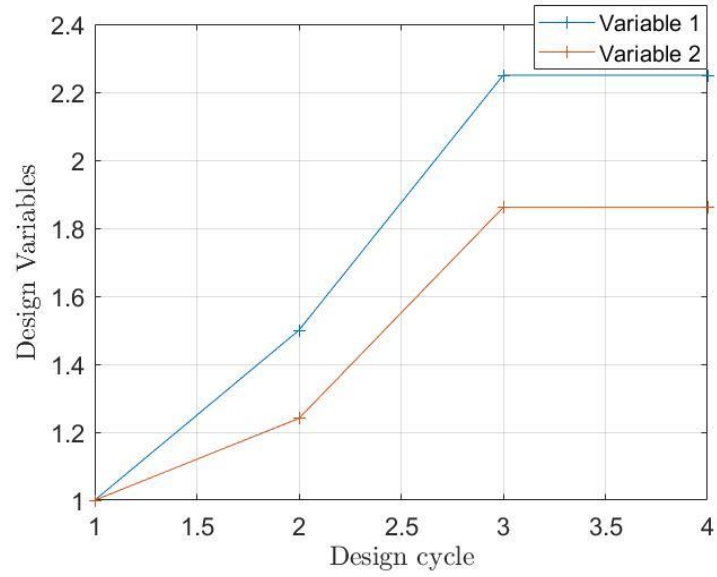
Figure 5.28 Design variables history of geometric boundary shape method.
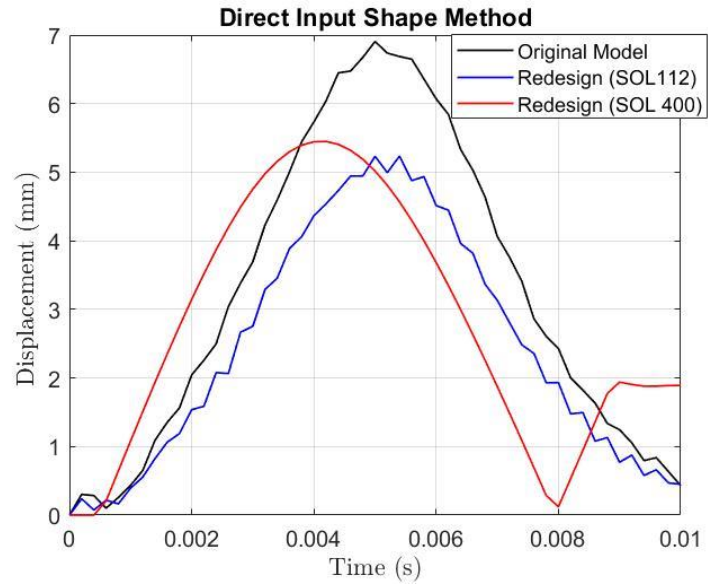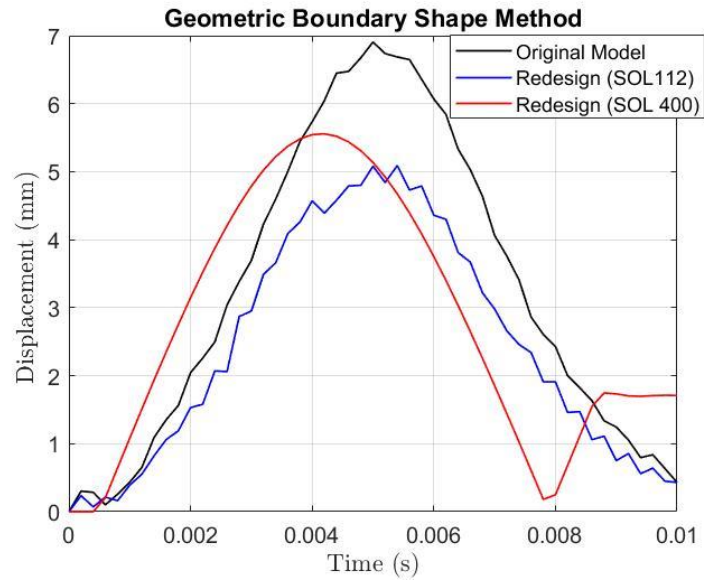

*Figure 5.29* Node 1 displacement comparison before and after shape optimization.
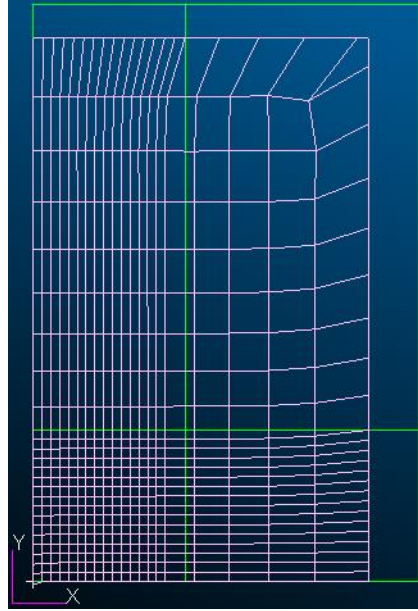
Figure 5.30 Composite plate before (green grids) and after (pink grids) geometric boundary shape optimization.

Table 5.5

Results of geometric boundary shape optimization using SOL 200

Property type	Initial value of the properties	Final value of the properties after 4 cycles
L	76.2 mm	71.89 mm
W	50.8 mm	44.55 mm
Objective m	11.62 g	9.63 g
Peak displacement δ	6.9 mm	5.11 mm (SOL 112), 5.56 mm (SOL 400)
CPU time: 68 s		
Total number of NASTRAN run of FEA: 5		

It is seen that both shape optimization methods were capable of leading the infeasible design converged into a feasible design space, which the size optimization failed to achieve. This serves as a base for the structural optimizations in real aerospace applications where the composite structures are much more complex. A variety of design variables need to be considered for each connected part, and the uncertain and changing impact loading would bring the determination of constraints to an open-end task.

6. Conclusions, Recommendation, and Future Works

In this thesis, the thin UD carbon fiber/epoxy composite laminates were fabricated to implement the low-velocity impact tests. The after-impact characteristics of the samples were measured by several responses. The numerical model was created in ABAQUS and validated with the experiments. At last, the sizing optimization methods and shape optimization methods coupled with the model in MSC. PATRAN/NASTRAN was applied to improve the damage resistance of the composite samples.

6.1. Conclusion

- After the LVI testing, the laminates showed better damage resistance using cylindrical impactor than hemispheric impactor. For the structural responses, the hemispheric impactor created larger deformation, and the former produced higher contact force. Also, the values changing of displacement, force, and impact energy from the simulation model matched well with the experimental data.

- The sample impacted by the hemispheric impactors presented fiber splitting on the backside and indentation on the front side. By applying the X-Ray micro-tomography technique, the failure results were successfully predicted by the intra-laminar damage model in ABAQUS. Also, it proved that the fiber damage and matrix damage are the dominant failure modes of thin laminates under LVI.

- Ahead of structural optimization, the validation between the models of SOL 400 and SOL 112 worked as expected. However, the difference between the linear and nonlinear analysis can't be neglected, the factors like the loading condition could only be approximated, and the choice of failure criteria would also challenge the accuracy of the results.

- Compared to the size optimization under linear dynamic loading, OpenMDAO was extremely time-consuming and it may easily fail if using improper parameters. However, OpenMDAO shows great potential in solving optimization with nonlinear loading, and it would give better results when applying to other less complex problems from previous studies.

- Although the sizing optimizations didn't get the desired converged results, the shape optimizations accomplished the goals. Therefore, shape optimization seems to be more capable of improving the damage resistance of the laminates under LVI. Furthermore, shape optimization is more difficult to model, and it calls for engineering intuition and experience of the researchers.

- Also, the shape optimization of changing the length and width of the plate was more effective than the size optimization that adjusted the ply thickness, this conclusion is based on using thin laminates. Thus, the preference for implementing the two optimization types should be further decided if using thick laminates.

6.2. Recommendations and Future Works

There were several contents in the presented work that could be improved and expanded to a wider research field. However, they are leaving as the recommendations and future works of this research because of the time limitation. Here, they are listing in below for reference:

- **Inter-Laminar Damage Modeling**

The thin laminates studied in this research mainly presented the impact damage on fiber and matrix, however, more laminates used in the aerospace industry are thicker, then delamination must be considered as the inter-laminar damage. Using the 3D solid

element in ABAQUS could simulate the inter-lamina damage by using the cohesive surface. The cohesive surfaces between the two consecutive layers are zero thickness, which helps to develop the ply-ply damage, like the initiation and evolution of the delamination, based on the Quadratic nominal stress criterion and the power-law fracture criterion. Those interface elements in ABAQUS could calculate the relative displacements of the "first" and "second" layer in terms of "tractions vs. displacement". Therefore, the possible inter-lamina delamination could be shown in the fringe plot and the damage evolution process could be obtained throughout the impact time.

- **Compression After Impact (CAI) Testing**

The "brooming" phenomena often happens when using the fixture, especially for the thin plates. It will create undesired failure modes at the outer edges of the compressed testing coupons, preventing the impacted plates to fracture through the impacted area. The author had performed the CAI test on the impacted samples, but they cracked on the boundary edges instead of in the middle area (impacted zone). This could be due to the thin laminates used. Some prior researchers have seen those unwanted failures on the plates with thickness less than 3 mm, and there is no confirmed ASTM test method or fixture to prevent the compressive failure modes at the ends (Sanchez-Saez et al., 2005). Therefore, more attempts are needed to test the thickness and the way of the fixture to get the desired crack in the impact zone, which means the plate should be fabricated with different thickness, then perform the LVI test again to get the impacted samples and adjust the screws when doing the CAI testing to get a proper fixture.

- **Composite Structure with Curvature**

A great deal of the research reviewed has been conducted on flat plate specimens. It can be argued that for most composite applications, especially in the aerospace and marine industry, composites will be utilized on curved structures such as laminated aircraft wings, horizontal/vertical stabilizer skins, and ship hulls, and therefore more work could be performed in this area.

- **Optimization Under Nonlinear Dynamic Impact Loading**

There are more accurate methods to redesign the structure under dynamic impact loading instead of the compromised solution of using linear transient loading. For example, the equivalent static loads (ESLs) method and response surface method (RSM) mentioned in Chapter 5 could be performed in Nastran to transform the non-linear dynamic response to an equivalent static load response. Although it would be more computational consuming but attain more accuracy which simulates the real loading condition. Except MSC. NASTRAN, other optimization software like Genesis and OptiStruct, are capable of nonlinear transient dynamic response optimization, which were mentioned in Chapter 2.

REFERENCES

Abir, M. R., Tay, T. E., Ridha, M., & Lee, H. P. (2017). Modelling damage growth in composites subjected to impact and compression after impact. *Composite Structures, 168*, 13-25.

Alemour, Belal, Badran, Omar, & Hassan, Mohd Roshdi. (2019). A Review of Using Conductive Composite Materials in Solving Lightening Strike and Ice Accumulation Problems in Aviation. *Journal of Aerospace Technology and Management*, *11*, e1919. Epub March 28, 2019.

Arora, J. (2012). Introduction to optimum design. New York: McGraw-Hill.

Birur, A. Time-Dependent Damage Evolution in Multidirectional Polymer Composite Laminates, Master Thesis, University of Manitoba, Canada, 2008.

Campbell, F. C. (2006). *Manufacturing technology for aerospace structural materials*. Kidlington; Amsterdam;: Elsevier.

Cantwell, W. J., Curtis, P. T., & Morton, J. (1984). Impact and subsequent fatigue damage growth in carbon fibre laminates. *International Journal of Fatigue, 6*(2), 113-118.

Caprino, G., Crivelli Visconti, I., & Di Ilio, A. (1984). Elastic behaviour of composite structures under low velocity impact. *Composites, 15*(3), 231-234.

Carrere, N., Laurin, F., & Maire, J. (2013). Micromechanical-based hybrid mesoscopic three-dimensional approach for non-linear progressive failure analysis of composite structures—Part B: Comparison with experimental data. *Journal of Composite Materials, 47*(6-7), 743-762.

Chang, F.-K., & Chang, K.-Y. (1987). A Progressive Damage Model for Laminated Composites Containing Stress Concentrations. *Journal of Composite Materials*, *21*(9), 834–855.

Choi, W., Kim, J., & Park, G. (2016). Comparison study of some commercial structural optimization software systems. *Structural and Multidisciplinary Optimization, 54*(3), 685-699.

Cook, L., Boulic, A., Harris, D., Bellamy, P and Irving, P.E. (2012). Reliability of Damage Detection in Advanced Composite Aircraft Structures. Safety Regulation Group, Civil Aviation Authority.

Farooq, U.; Gregory, K. (2009). Finite Element Simulation of Low Velocity Impact Damage Morphology in Quasi-Isotropic Composite Panels under Variable Shape Impactors, *European Journal of Scientific Research*, 25(4), 636-648.

García-Rodríguez, S. M., Costa, J., Bardera, A., Singery, V., & Trias, D. (2018). A 3D tomographic investigation to elucidate the low-velocity impact resistance, tolerance and damage sequence of thin non-crimp fabric laminates: Effect of ply-thickness. *Composites. Part A, Applied Science and Manufacturing, 113*, 53-65.

Going to extremes: Meeting the emerging demand for durable polymer matrix composites. (2005). *Jom (1989), 57*(9), 13.

Gower, H. L., Cronin, D. S., & Plumtree, A. (2008). Ballistic impact response of laminated composite panels. *International Journal of Impact Engineering, 35*(9), 1000-1008.

Gray, J. S., Hwang, J. T., Martins, Joaquim R. R. A, Moore, K. T., & Naylor, B. A. (2019). OpenMDAO: An open-source framework for multidisciplinary design, analysis, and optimization. *Structural and Multidisciplinary Optimization, 59*(4), 1075-1104.

Guillamet, G., Turon, A., Costa, J., Renart, J., Linde, P., & Mayugo, J. A. (2014). Damage occurrence at edges of non-crimp-fabric thin-ply laminates under off-axis uniaxial loading. *Composites Science and Technology, 98*, 44-50.

Hampson, P. R., & Moatamedi, M. (2007). A review of composite structures subjected to dynamic loading. *International Journal of Crashworthiness, 12*(4), 411-428.

Hashin, Z., & Rotem, A. (1973). A Fatigue Failure Criterion for Fiber Reinforced Materials. Journal of Composite Materials, 7(4), 448–464.

Hull, D., & Clyne, T. W. (1996). *An introduction to composite materials* (Second ed.). Cambridge;New York;: Cambridge University Press.

Hwang, J., & Martins, J. (2018). A computational architecture for coupling heterogeneous numerical models and computing coupled derivatives. *ACM Transactions on Mathematical Software (TOMS), 44*(4), 1-39.

Johnson, T. C., Kirches, C., & Wächter, A. (2015). An active-set method for quadratic programming based on sequential hot-starts. *SIAM Journal on Optimization, 25*(2), 967-994.

Kassapoglou, C. (2013). Design and analysis of composite structures: With applications to aerospace structures (2nd edition). Chichester [England]: John Wiley & Sons Inc.

Kreculj, D., & Rasuo, B. (2013). Review of impact damages modelling in laminated composite aircraft structures. *Tehnicki Vjesnik-Technical Gazette, 20*(3), 485-495.

Kumar, P., & Rai, B. (1993). Delaminations of barely visible impact damage in CFRP laminates. *Composite Structures, 23*(4), 313-318.

Kuo, Y. -., Lin, H. -., Wang, C. -., & Liao, C. -. (2007). Estimating the elastic modulus through the thickness direction of a uni-direction lamina which possesses transverse isotropic property. *Journal of Reinforced Plastics and Composites*, *26*(16), 1671-1679.

Lapczyk, I., & Hurtado, J. A. (2007). Progressive damage modeling in fiber-reinforced materials. *Composites. Part A, Applied Science and Manufacturing, 38*(11), 2333-2341.

Lee, J., & Park, G. (2011). Shape optimization of the initial blank in the sheet metal forming process using equivalent static loads. *International Journal for Numerical Methods in Engineering, 85*(2), 247-268.

Leylek, Z., Scott, M. L., Georgiadis, S., & Thomson, R. S. (1999). Computer modelling of impact on curved fibre composite panels. *Composite Structures, 47*(1), 789-796.

Liu, P. F., Liao, B. B., Jia, L. Y., & Peng, X. Q. (2016). Finite element analysis of dynamic progressive failure of carbon fiber composite laminates under low velocity impact. *Composite Structures, 149*, 408-422.

Madjidi, S., Arnold, W. S., & Marshall, I. H. (1996). Damage tolerance of CSM laminates subject to low velocity oblique impacts. *Composite Structures, 34*(1), 101-116.

Maio, L., Monaco, E., Ricci, F., & Lecce, L. (2013). Simulation of low velocity impact on composite laminates with progressive failure analysis. *Composite Structures, 103*, 75-85.

MSC Nastran user's guide design sensitivity and optimization version 2017 (2017b) MSC Software Co., Santa Ana, CA, US, 11-12.

Pavier, M. J., & Clarke, M. P. (1995). Experimental techniques for the investigation of the effects of impact damage on carbon-fibre composites. *Composites Science and Technology, 55*(2), 157-169.

Pietropaoli, E., & Pietropaoli, E. (2012). Progressive failure analysis of composite structures using a constitutive material model (USERMAT) developed and implemented in ANSYS. *Applied Composite Materials, 19*(3), 657-668.

Puck, A., & Schürmann, H. (2002). Failure analysis of FRP laminates by means of physically based phenomenological models. *Composites Science and Technology, 62*(12-13), 1633-1662.

Raju, K. S., Smith, B. L., Tomblin, J. S., Liew, K. H., & Guarddon, J. C. (2008). Impact damage resistance and tolerance of honeycomb core sandwich panels. *Journal of Composite Materials, 42*(4), 385-412.

Ross, C. A., & Sierakowski, R. L. (1973). Studies on the impact resistance of composite plates. *Composites, 4*(4), 157-161.

Sanchez-Saez, S., Barbero, E., Zaera, R., & Navarro, C. (2005). Compression after impact of thin composite laminates. *Composites Science and Technology, 65*(13), 1911-1919.

Sasikumar, A., Trias, D., Costa, J., Blanco, N., Orr, J., & Linde, P. (2019). Effect of ply thickness and ply level hybridization on the compression after impact strength of thin laminates. *Composites. Part A, Applied Science and Manufacturing, 121*, 232-243.

Schmit LA, (1960) Structural design by systematic synthesis. Proceedings of the second ASCE conference, 105–122.

Shah, S. Z. H., Karuppanan, S., Megat-Yusoff, P. S. M., & Sajid, Z. (2019). Impact resistance and damage tolerance of fiber reinforced composites: A review. *Composite Structures, 217*, 100-121.

Shi Y. Modelling low velocity impact behaviour of composite laminates used in aerospace. PhD Dissertation, the University of Sheffield, 2014.

Soutis, C. (2005). Fibre reinforced composites in aircraft construction. *Progress in Aerospace Sciences, 41*(2), 143-151.

Sun, M., Chang, M., Wang, Z., Li, H., & Sun, X. (2018). Experimental and simulation study of low-velocity impact on glass fiber composite laminates with reinforcing shape memory alloys at different layer positions. *Applied Sciences, 8*(12), 2405.

Talreja, R. (2006). Multi-scale modeling in damage mechanics of composite materials. *Journal of Materials Science, 41*(20), 6800-6812.

Thomas, W. F. (1973). Factors affecting the impact strength of glass-fibre-reinforced polyester composites. *Composites, 4*(3), 105-110.

Tsai, S. W., & Wu, E. M. (1971). A General Theory of Strength for Anisotropic Materials. *Journal of Composite Materials*, *5*(1), 58–80.

Xiaoquan, C., Al-Mansour, A., & Zhengneng, L. (2009). Residual strength of stitched laminates after low velocity impact. *Journal of Reinforced Plastics and Composites, 28*(14), 1679-1688.

Yokozeki, T., Aoki, Y., & Ogasawara, T. (2008). Experimental characterization of strength and damage resistance properties of thin-ply carbon fiber/toughened epoxy laminates. *Composite Structures, 82*(3), 382-389.

APPENDIX A – CFRP Prepreg Material (HEATCON Composite, Tukwila, WA)

The following Figure provides the material properties and fabrication requirements of the composite prepreg used in this research.

'TORAY' 3900 **TORAYCA**
Toray Composite Materials America, Inc.

LAMINA/LAMINATE MECHANICAL PROPERTIES: UD T800S-24K - COMMERCIAL READY

PROPERTY	SYMBOL	METHOD	UNITS	CTA	RTA
0° Tensile Strength	F_{1t}	ASTM D3039	ksi (MPa)	410 (2830)	430 (2965)
90° Tensile Strength	F_{2t}	ASTM D3039	ksi (MPa)	8.25 (56.9)	8.75 (60.3)
0° Tensile Modulus	E_{1t}	ASTM D3039	Msi (GPa)	21.5 (148)	21.5 (148)
90° Tensile Modulus	E_{2t}	ASTM D3039	Msi (GPa)	1.40 (9.7)	1.20 (8.3)
0° Compressive Strength	F_{1c}	ASTM D6641	ksi (MPa)	257 (1772)	258 (1779)
90° Compressive Strength	F_{2c}	ASTM D6641	ksi (MPa)	44.0 (303)	31.0 (214)
0° Compressive Modulus	E_{1c}	ASTM D6641	Msi (GPa)	19.0 (131)	19.0 (131)
90° Compressive Modulus	E_{2c}	ASTM D6641	Msi (GPa)	1.40 (9.7)	1.20 (8.3)
In-Plane Shear Strength @ 5% or Ultimate	F_{12}	ASTM D3518	ksi (MPa)	13.0 (89.6)	10.0 (68.9)
In-Plane Shear Modulus	G_{12}	ASTM D3518	Msi (GPa)	0.700 (4.83)	0.570 (3.93)
Short Beam Shear Strength	SBS	ASTM D2344	ksi (MPa)	20.0 (138)	14.0 (96.5)
Poisson's Ratio	v_{12}	ASTM D3039	-	-	0.33
Poisson's Ratio	v_{21}	ASTM D3039	-	-	0.02
Open Hole Tension Strength (25/50/25)	OHT	ASTM D5766	ksi (MPa)	-	73 (503)
Open Hole Compression Strength (25/50/25)	OHC	ASTM D6484	ksi (MPa)	-	43 (296)
Compression After Impact (25/50/25)	CAI	ASTM D7137	ksi (MPa)	-	42
Cured Ply Thickness	CPT	-	in. (mm)	0.0075 (0.191)	

Tension and compression values are normalized to the indicated CPT herein.

Notes:
CTA: -65°F (-54°C), Ambient
RTA: 72°F (22°C), Ambient
ETW: 180°F (82°C) Ambient, Conditioned at 160°F/85% RH until equilibrium

TORAY

Toray Composite Materials America, Inc.

3900

TORAYCA

BAGGING PROCEDURE

- Air Pathway Material (Encompassing the Part)
- Edge Breather
- Vacuum Seal Tape
- Vacuum Bag
- Surface Breather
- Non-Perforated Release Film
- Prepreg
- Non-Perforated Release Film (optional)
- Tool

STORAGE LIFE

Out Life*	42 days @ 75 °F
Freezer Life	24 months @ <10 °F

*Tack and drape is optimum at 72F and 65% RH

CURE CYCLE - AUTOCLAVE

1. Apply full vacuum (minimum of 22"Hg (74.5 kPa) at sea level) to the vacuum bag assembly and check for leak prior to the beginning of the cure cycle. The leak rate shall be less than 2.0" Hg (6.77 kPa) over 5 minutes
2. Apply 85 + 15/-0 psi (586 + 103/-0 kPa) autoclave pressure to the laminate.
3. Vent the vacuum bag when the autoclave pressure reaches 20psi (138 kPa)
4. Apply the temperature ramp to 350 ± 10°F (177 ± 5°C) at rate of 3.0 ± 2.0 °F (1.7 ± 1.1°C) per minute.
5. Maintain the cure temperature at 350 ± 10°F (177 ± 5°C) for 120 - 180 minutes.
6. Cool vessel to 140°F (60°C) or lower at a maximum rate of 5°F (2.78°C) per minute before removing pressure.
7. Remove the bagged panels from the curing vessel.